REVIEW

Robotically Steered Needles: A Survey of Neurosurgical Applications and Technical Innovations

This article was published in the following Dove Press journal:
Robotic Surgery: Research and Reviews

Michel A Audette [1]
Stéphane PA Bordas [2]
Jason E Blatt [3]

[1]Department of Computational Modeling and Simulation Engineering, Old Dominion University, Norfolk, VA, USA; [2]Institute of Computational Engineering, University of Luxembourg, Faculty of Sciences Communication and Technology, Esch-Sur-Alzette, Luxembourg; [3]Department of Neurosurgery, University of Florida, Gainesville, FL, USA

Abstract: This paper surveys both the clinical applications and main technical innovations related to steered needles, with an emphasis on neurosurgery. Technical innovations generally center on curvilinear robots that can adopt a complex path that circumvents critical structures and eloquent brain tissue. These advances include several needle-steering approaches, which consist of tip-based, lengthwise, base motion-driven, and tissue-centered steering strategies. This paper also describes foundational mathematical models for steering, where potential fields, nonholonomic bicycle-like models, spring models, and stochastic approaches are cited. In addition, practical path planning systems are also addressed, where we cite uncertainty modeling in path planning, intraoperative soft tissue shift estimation through imaging scans acquired during the procedure, and simulation-based prediction. Neurosurgical scenarios tend to emphasize straight needles so far, and span deep-brain stimulation (DBS), stereoelectroencephalography (SEEG), intracerebral drug delivery (IDD), stereotactic brain biopsy (SBB), stereotactic needle aspiration for hematoma, cysts and abscesses, and brachytherapy as well as thermal ablation of brain tumors and seizure-generating regions. We emphasize therapeutic considerations and complications that have been documented in conjunction with these applications.

Keywords: deep-brain stimulation, stereoelectroencephalography, intracerebral drug delivery, brain biopsy, stereotactic needle aspiration, brachytherapy, needle steering

Introduction

There is a growing emphasis on both minimally invasive and robotically assisted therapies in neurosurgery. An important class of minimally invasive neurosurgical therapies exploit needle-based delivery mechanisms, which include the positioning of electrodes in deep brain stimulation (DBS)[1] and stereoelectroencephalography (SEEG),[2] intracerebral drug delivery (IDD),[3] stereotactic brain biopsy (SBB),[4] stereotactic needle aspiration for hematoma, cysts and abscesses,[5] and brachytherapy[6] as well as thermal ablation[7,8] of brain tumors and seizure-generating regions. Meanwhile, surgical robotics have also emerged over the past two decades, thereby endowing surgeons with improved precision, stability and control, in a manner that potentiates minimally invasive approaches. This paper represents a survey of the techniques as well as clinical applications at the intersection of robotic surgery and needle-based neurological therapies.

Robotically Steered Surgical Needles
Overview

This paper will apprise the reader of the considerable breadth of neurosurgical applications of needle-based therapies, as well as leading technical solutions in this area. It consists of a

Correspondence: Michel A Audette
Department of Computational Modeling and Simulation Engineering, Old Dominion University, Norfolk, 5115 Hampton Blvd, Norfolk, VA, USA
Email maudette@odu.edu

survey of technical innovations followed by an overview of clinical applications. As will be evident, there is a dichotomy separating the clinical and engineering communities. Broadly speaking, surgeons currently tend to emphasize simple linear paths that are intuitive to understand and to plan. Meanwhile, as will be evident in the following section, emerging robotic approaches are not constrained by this emphasis on linearity and pushing the envelope in a manner that will enable critical tissue-sparing curvilinear paths to surgical targets. Steered needles enable curvilinear shapes that make it possible to achieve highly precise, complex paths to the target that have the inherent flexibility to avoid critical tissues or highly eloquent areas of the brain. Better outcomes could result in part through better accuracy as well as precision in the targeting itself, reducing the rate of false negatives from a biopsy, focusing the delivery of radioactive seeds in brachytherapy, or restricting thermal ablation of cancerous tissue rather than spilling onto healthy tissue. Moreover, outcomes could also be improved by integrating image guidance, which can entail critical tissue maps from angiographic imaging or metabolic insight through fMRI, PET or SPECT, and coupling to robotic delivery through suitable path planning.

Because of the complexity of curvilinear path planning, in terms of integrating myriad 3D anatomical morphologies and multi-modal tomographic images, possibly segmented automatically, as well as the dexterity needed to thread a dynamically configurable curved needle along an elaborate planned path, the clinical penetration of steered needles increasingly presupposes robotic control, albeit with human-in-the-loop expert supervision. Despite this overhead, as suggested by Okamura and her collaborators,[9,10] the adoption of these technologies could very well be justified through the ability to use steerable needles to deliver therapy to otherwise unreachable targets within a minimally invasive surgical framework.

The next section will survey the main innovations in the design and robotic control of steerable needles, as well as medical imaging trends that will affect the path planning. For a detailed survey of steerable needle design, the reader should consult the survey by Cowan.[10] As depicted in Figure 1, steerable robots can exploit and possibly combine several techniques for controlling the needle position during the intervention. The needle can be steered to a target by generating forces using an asymmetric tip, using a pre-curved needle whose curvature is controllable, by lateral manipulation, as well as deforming nearby tissue to push the tissue-based target into the needle's path.[10] In addition, a steerable external cannula can further provide dexterity prior to and during insertion. Moreover, as shown in Figure 2, the basic architecture of a robotic component of the needle-steering system is comprised of physical and computerized elements. The physical setting is comprised of the needle-steering robotic system, the patient and the clinician, while the computerized elements center on medical image analysis (imaging, segmentation, meshing) as well as surgery planning, and finally robotic control.

Just as the dexterity needed to control the precise path of a curvilinear needle increasingly presupposes a computerized robotic approach, anatomical variability among patients is significant enough that it is equally unlikely to determine a surgical approach without descriptive surgery planning based on tomographic imaging in its various guises, such as MRI, CT, or possibly ultrasound. This surgery planning typically cannot proceed from raw MRI or CT, and generally
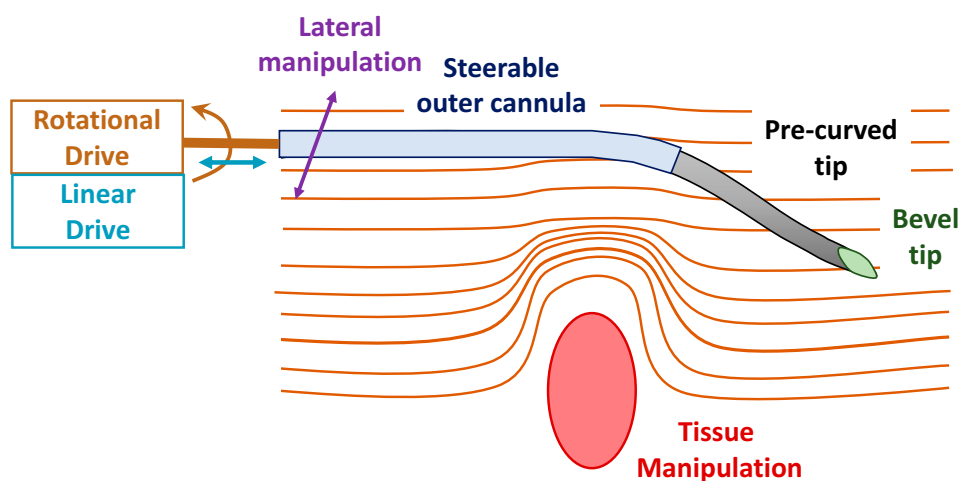

Figure 1 Summary of techniques applied to needle steering, emphasizing the asymmetric (eg, bevel) tip, pre-curved needle segments, steerable outer cannula, independent tissue manipulation, lateral manipulation, and positioning based linear or rotational motion, as defined in relation to the needle central axis. Data from Cowan et al.[10]
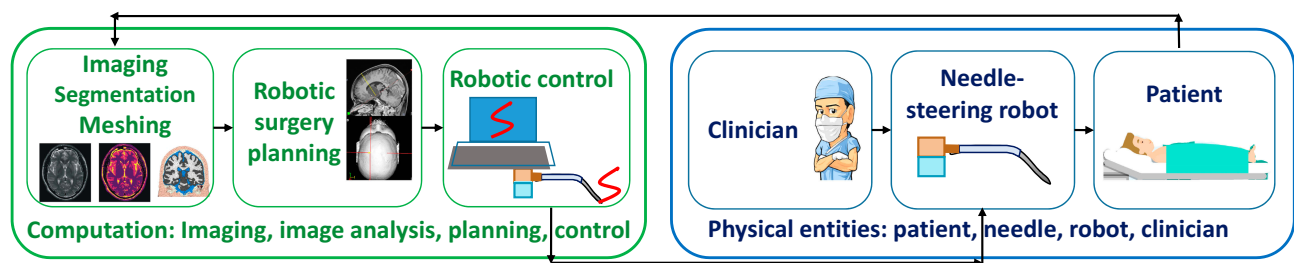
2

Robotic Surgery: Research and Reviews 2020:7

Figure 2 Basic architecture of needle-steering robotic system. Data from Cowan et al.[10] The left side, depicted in green integrates all computerized components: medical imaging and image analysis, surgery planning and robotic control. Imaging can also occur intraoperatively, leading to anatomy update. The right side depicts physical entities: the surgeon, robot and needle, as well as the patient.

requires a segmentation step that makes explicit the anatomical structures relevant to the procedure. These anatomical structures include healthy and pathological brain tissue, cerebrovasculature, DTI/HARDI-based white matter tracts, and highly eloquent brain regions derived from fMRI, PET or SPECT, just to name a few options. Furthermore, in many cases, because of the potentially degrading effect of brain shift on the robot-image transformation, an intraoperatively updated anatomical model may be vital to maintaining the accuracy of the robotic navigation. The intraoperative update requirement may in turn impose a minimally supervised (or unsupervised) meshing stage downstream of the segmentation, thereby enabling volumetric interpolation, typically based on finite elements.[11,12] As noted in the first author's survey,[13] the meshing stage can either be structured, e.g. building on hexahedra of constant connectivity, or unstructured, i.e. based on tetrahedra whose connectivity varies at every vertex. There are pros and cons for each meshing approach, where tetrahedralization benefits from unsupervised algorithms.

Needle-Steering Approaches

The following section provides an overview of competing techniques for achieving controlled curvilinear paths within the patient, with an emphasis on the subset of such techniques particularly relevant to neurosurgical applications. Broadly speaking, these techniques fall under the following categories:

flexible needles, bevel shape and asymmetry, pre-bent needle segments, tissue manipulation, and actuation of the needle base, as depicted in Figure 1.

Needles typically used in therapy can be classified as either symmetric or asymmetric; the former consist of conically or prismatically tipped needles, while the latter are beveled. Clinicians experienced at needle insertion know that beveled tip needles tend to bend as a result of their tip asymmetry, in comparison with symmetrically tipped needles. As depicted in Figure 3, the beveled shape produces forces at the needle–tissue interface that imparts a bending force on the needle during insertion. The resulting flexing may be reduced either by increasing the stiffness of the needle or by spinning it, in a drill-like motion, during insertion. In contrast with traditional needle therapies that seek to limit the bending motion, surgical robotics research tends to emphasize and exploit this deformation for novel approaches to therapy delivery, the technique referred to as needle steering. One of the main techniques in needle steering is founded on the asymmetry of the tip, which involves either a beveled termination of Figure 3B or a composite of a beveled tip and pre-curved segment to the needle as depicted in Figure 3C.

Tip-Based Steering

The most basic approach to needle-steering exploits the beveled tip, which is simple to manufacture and straightforward to control, compared to the other approaches described in this
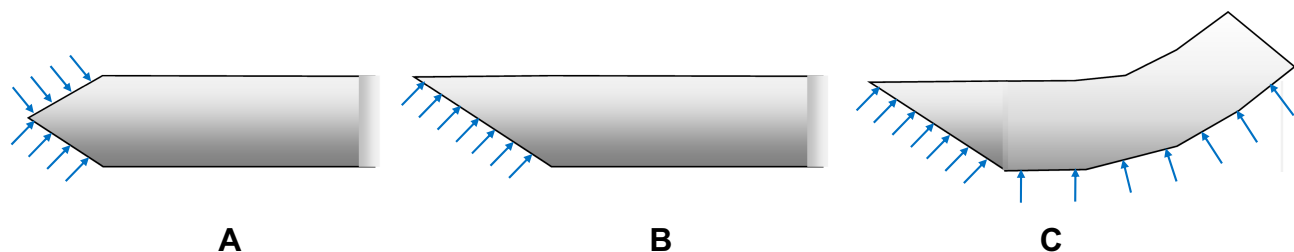

Figure 3 Needle tip shapes featuring (**A**) a symmetric and cone-shaped tip, (**B**) an asymmetric beveled tip. (**C**) Combination of bevel tip and pre-bent needle shape. Data from Cowan et al.[10]

section. Steering a basic bevel-tip needle is intuitive enough to enable manual control, based on a combination of insertion, which naturally induces a curved path through asymmetric forces, as shown in Figure 3, and rotating the needle about its central axis, which alters the bending orientation.[14] The comparative advantage of the bevel-tip approach over others is its simplicity, which makes it amenable to either manual or robotic control, while making possible a combination of the two as a result.

Webster et al[14] described the bevel-tip needle as a model with insertion and rotation speeds as the main inputs to a nonholonomic kinematics model based on an analogy with a bicycle having a locked front wheel of angle ϕ and a wheel base l_1 as depicted in Figure 4. A robot is said to be holonomic if all the constraints to which it is subjected are integrable as positional constraints of the form $f(q_1, q_2, \cdots, q_n, t) = 0$; a robot whose system constraints cannot be written in this integrable form is said to be nonholonomic. The first wheel angle ϕ and first parameter l_1 determine the curvature κ of the needle direction, while parameter l_2 determines the location along the bicycle that is attached to the needle tip, labeled n. According to this model, insertion of the needle at speed u_1 equates with riding the bicycle along a circular arc of radius $1/\kappa$, while spinning the needle at a speed u_2 orients the plane in which the bicycle's path is embedded.[14] Through suitable simplifications that dispense with l_2 while retaining curvature κ, the two-parameter bicycle can be reduced to a single-parameter unicycle, whose wheel located at the needle tip. This unicycle model's simplicity and fidelity made it suitable for the design of control systems.[15]

This amount of curvature can be modulated, in conjunction with a duty cycle strategy to further adjust the needle path, as demonstrated by Webster as well as applied by Engh et al to neurosurgery, and as depicted in Figure 5.[3] In other words, a beveled needle that is constantly spinning will eliminate the asymmetric forces on it that cause it to flex, resulting in a straight insertion path, while a complete absence of spinning (0% duty cycle) entails a maximally curved path. In between these two poles, a 50–50 duty cycle results in a curved path halfway in between the straight line corresponding to 100% duty cycle and the maximally flexed path resulting from the absence of spin. The intuitive response afforded by this rotational modulation approach enabled practical neurosurgical applications, as demonstrated by Engh.[3]

Lengthwise Steering

A technique complementary to the preceding is a curved, pre-bent shape, as shown in Figure 3C,[15] which can be controlled like a straight bevel-tipped needle. The radius of curvature of pre-bent needles varies with needle length and degree of asymmetry.[10] Moreover, it is also feasible to modulate needle curvature by varying the curvature of the tip. A method for controlling tip curvature includes the application of tiny wires, such as shape memory alloy (SMA) wires as proposed by Konh,[16] to flexibly configure the needle tip. An alternate approach consists of constraining the curved needle, or stylet, within a stiff hollow cannula that surrounds portions of the stylet, as proposed by Okazawa.[17] By covering the bent section of the stylet within the cannula, the stiffer covering has the effect of straightening out the aggregate shape of the needle. The deflection at the tip, in relation to the needle shaft, can therefore be controlled by varying the uncovered portion of the stylet that penetrates the tissue. In other words, the length of needle protrusion is variable and determines the curvature of the tissue-embedded needle. This sheath concept generalizes to the concentric-tube robot: a suite of concentric flexible tubes that cooperatively impart an arbitrary 3D path to the robot.[18,19] One of the main advantages of curved needles over the simple bevel-tip needle is that they can achieve a smaller radius of curvature through a larger perpendicular force. Possible limitations include the reliance on automated control due to a lack of intuitive manual control mode, especially where the deployment of concentric tubes is concerned, as well as a possible deviation of clinical behavior of the cannula from the laboratory predictions, due to factors such as the presence of fluids (e.g. corticospinal fluid, blood).

Base Motion-Driven Steering

As proposed by DiMaio and Salcudean,[20] movement of the needle base, perpendicular to insertion axis, offers an alternate option for positioning the needle tip. The perpendicular base
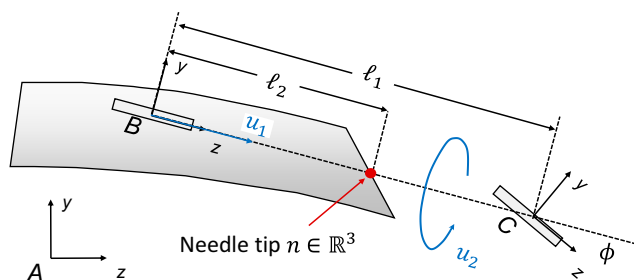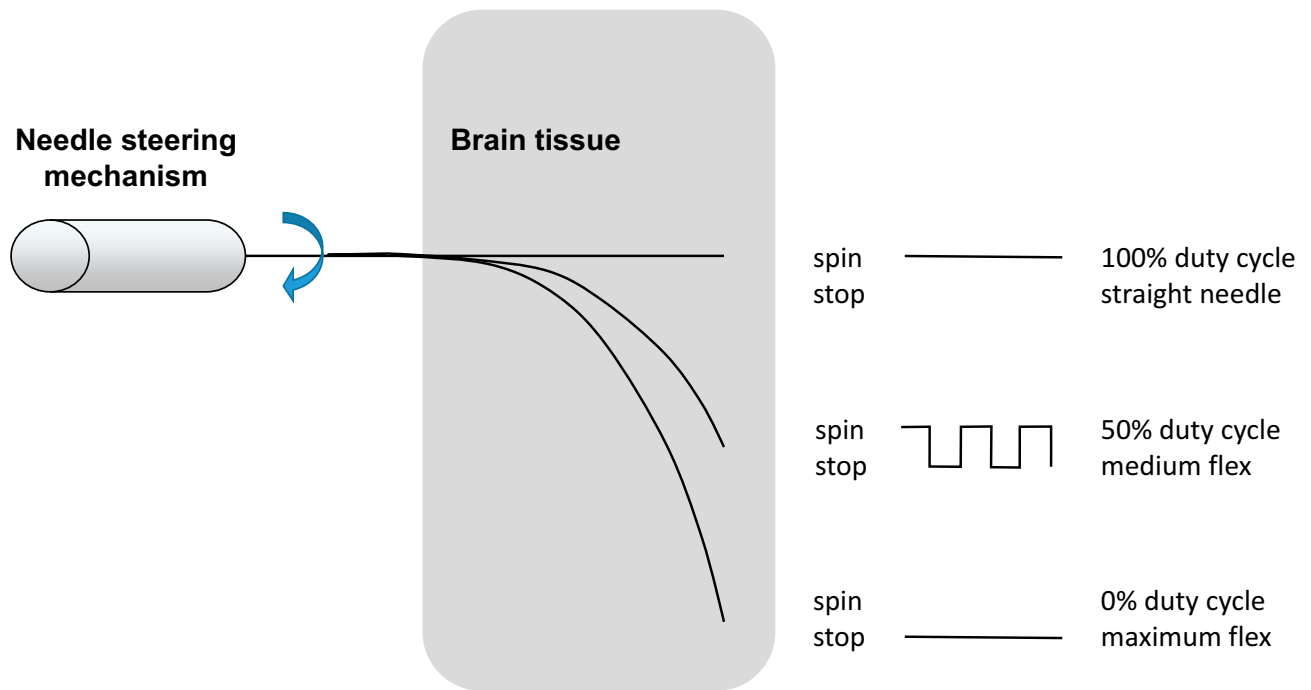

Figure 4 Webster's nonholonomic model of beveled tip needle emphasizing a pair of bicycle "wheels" at frames B and C. The x coordinate axes for frames (**A, B** and **C**) are pointing into the page. Data from Winters et al[23] and Cowan et al.[10]

4

Robotic Surgery: Research and Reviews 2020:7

Figure 5 Relationship between spinning duty cycle of beveled needle and its induced flexion. Data from Engh et al.[3]

motions result in motion of the needle shaft within the tissue whereby the needle pivots analogously to a beam about a tissue-centered fulcrum.[10] DiMaio developed a model of the needle tip expressed in terms of the motion applied to the base, as depicted in Figure 6, termed the needle manipulation Jacobian. In 2D, this model represented the relationship between translational and rotational velocities of the needle tip and base, $\begin{bmatrix} \dot{x}_t \ \dot{y}_t \ \dot{\theta}_t \end{bmatrix}^T$ and $\begin{bmatrix} \dot{x}_b \ \dot{y}_b \ \dot{\theta}_b \end{bmatrix}^T$, encoded in a 3x3 matrix J that depends on needle and tissue configuration parameters q_k:

$$J(q_k) = \begin{bmatrix} \frac{\partial x_t}{\partial x_b} & \frac{\partial x_t}{\partial y_b} & \frac{\partial x_t}{\partial \theta_b} \\ \frac{\partial y_t}{\partial x_b} & \frac{\partial y_t}{\partial y_b} & \frac{\partial y_t}{\partial \theta_b} \\ \frac{\partial \theta_t}{\partial x_b} & \frac{\partial \theta_t}{\partial y_b} & \frac{\partial \theta_t}{\partial \theta_b} \end{bmatrix} \quad (1)$$

The velocity relationship was written in terms of infinitesimal changes in position based on this Jacobian:

$$\begin{bmatrix} \Delta x_t \ \Delta y_t \ \Delta \theta_t \end{bmatrix}^T \approx J(q_k) \begin{bmatrix} \Delta x_b \ \Delta y_b \ \Delta \theta_b \end{bmatrix}^T \rightarrow as \rightarrow \Delta x_b \ \Delta y_b \ \Delta \theta_b \rightarrow 0 \quad (2)$$
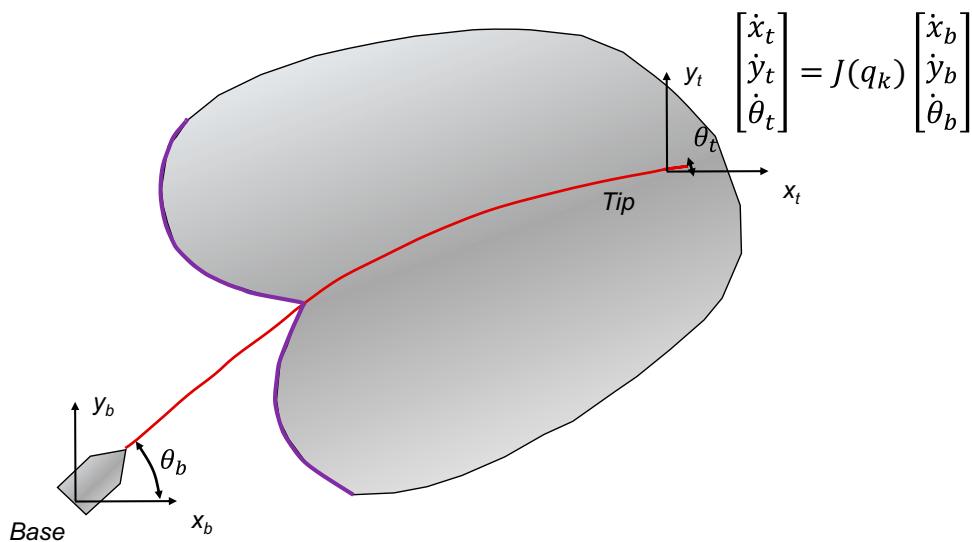

$$\begin{bmatrix} \dot{x}_t \\ \dot{y}_t \\ \dot{\theta}_t \end{bmatrix} = J(q_k) \begin{bmatrix} \dot{x}_b \\ \dot{y}_b \\ \dot{\theta}_b \end{bmatrix}$$

Figure 6 Needle manipulation Jacobian model for expressing tip motion in relation to base translation and rotation. Data from DiMaio et al.[19]

DiMaio noted that an analytical expression for J is typically not feasible due to the complexity of the interactions between the needle and the tissue, but suggested a numerical approach to estimating the Jacobian matrix from simple perturbations $[\Delta x_b \; 0 \; 0]^T$, $[0 \; \Delta y_b \; 0]^T$ and $[0 \; 0 \; \Delta \theta_b]^T$ applied to the needle base.

One of the limitations of the preceding methods is analysis needed to produce stable Jacobian results, given the sensitivity of derivatives to noise-related variation; DiMaio required a finite element method (FEM) approach that restricts the application to offline planning rather than interactive simulation. An accelerated base-centered model was proposed by Glozman and Shoham, whereby steering a flexible bevel-tip needle into soft tissue could be stated as a problem of inverse kinematics, ie, assuming that we have the position and orientation of the tip trajectory, one can derive the implied translation and orientation of the base of the needle.[21] The Glozman model is described at length in the Beam Models section.

Tissue-Centered Positioning Strategies

In addition to the needle-centered steering strategies, one can also manipulate the surrounding tissue to reposition targeted points of the tissue into the path of the needle or alternately nudge critical tissues away from the needle's trajectory. Mallapragada et al proposed a robotic breast tumor therapy delivery system based on three actuators that compress the tissue in a manner that results in the precise motion needed to put a tumor on the needle tip, without directly repositioning the needle itself.[22] This tissue-centered approach has limited relevance to neurosurgery for two reasons. First, the rigid cranium prevents similar actuation on brain parenchyma, notwithstanding the considerable damage to functionally vital brain tissue that is likely to occur. Second, the fibrous nature of breast tumors may be consistent with tissue indentation in their proximity, but the same manipulation near a brain tumor can result in iatrogenic dispersion of tumor tissue, especially if a significant portion of tumor tissue is viscous liquid.[23] In short, this approach is not a solution that generalizes to most clinical applications, least of all to neurosurgery, even if (somewhat) feasible for breast procedures.

Steering Models

Beyond the broad strategies for needle steering described in earlierFpote, we can also allude to a variety of mathematical models, including potential fields, nonholonomic models, and virtual spring models.

Potential Fields for Path Planning

DiMaio and Salcudean proposed a method for robotic needle path planning and obstacle based on a potential field defined over a configuration space. Path planning was envisioned as an optimization of a potential energy function that combines an attraction of the path towards a target and a repulsion that nudges the needle path away from obstacles such as critical tissues.[20] This potential field is defined over a configuration space $\mathcal{C}$ parametrized according to the position and the orientation in 2D of the tip of the needle, within the tissue domain, as depicted in Figure 7A. Obstacles are represented in regions in $\mathcal{C}$-space known as $\mathcal{C}$-obstacles and denoted $\mathcal{CB}$. Motion planning is described as the determination of a satisfactory trajectory from the initial configuration q_0 to a desired configuration q_{goal} within $\mathcal{C} - \mathcal{CB}$. A parabolic potential well of attraction, $\hat{U}(q_k)$, as defined in expression (3), is located at the target.

$$\check{U}(q_k) = \frac{1}{2}k\left\|q_k - q_{goal}\right\|^2 \qquad (3)$$

where k is a scale parameter and where all $q_k \epsilon \mathcal{C}$. This potential well $\hat{U}$ is assumed to have a minimum at $q_{goal} \epsilon \mathcal{C}$ and is assumed positive everywhere else, while increasing monotonically from q_{goal}. We can define the gradient of the potential function $\check{U}$, which is interpreted as a generalized attraction force $\hat{F}$

$$\check{F}(q_k) = -\nabla \check{U}(q_k) = \frac{1}{2}k\left(q_k - q_{goal}\right) \qquad (4)$$

where for a 2D tissue domain, $q_k, q_{goal} \in \mathbb{R}^3$ and include an orientation component. The path planning also imbeds a repulsive potential, such as shown in Figure 7B, defined about each obstacle:

$$\hat{U}(q_k) = \begin{cases} \frac{1}{2}\eta\left(\frac{1}{\rho} - \frac{1}{\rho_0}\right), & if \, \rho \leq \rho_0 \\ 0, & if \, \rho > \rho_0 \end{cases} \qquad (5)$$

A total generalized repulsion force is defined in a manner that includes the gradient of the repulsive potential in (5) $\nabla\hat{U}$ and an orientational component defined as a repulsive torque τ:

$$\hat{F}(q_k) = \begin{bmatrix} \nabla\hat{U}(q_k) \\ \tau(q_k) \end{bmatrix} \qquad (6)$$

The combined effect of attractive and repulsive potentials attracts the tip of the needle to the target, while enabling it to
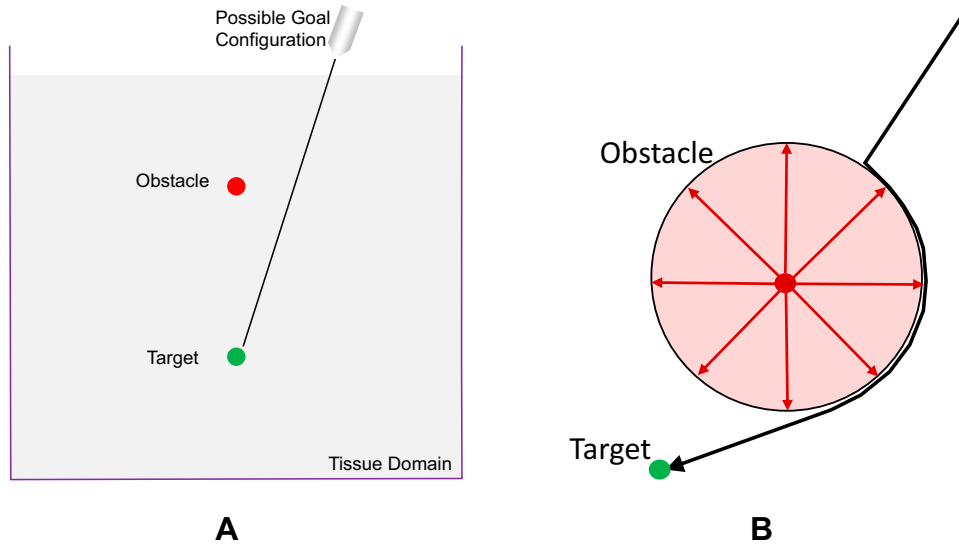
Figure 7 DiMaio's potential field formalism. (**A**) Tissue-spanning 2D domain with embedded target and obstacle components. A multiplicity of starting and goal positions are feasible. (**B**) Example of repulsive obstacle: circular repulsion potential. Data from Rucker et al.[19]

circumvent obstacles. To optimize this aggregate potential function, the corresponding base motion ΔQ_b is computed based on the normalized sum of expressions (4) and (6), which is combined needle with the Jacobian of expression (1) and a weighting matrix W:

$$\Delta Q_b = J^{-1}\left(W\frac{\left(\check{F}(q_k) + \hat{F}(q_k)\right)}{\left\|\check{F}(q_k) + \hat{F}(q_k)\right\|}\right) \qquad (7)$$

While this approach has promise, the calculation of repulsive fields presupposes detailed patient-specific models of critical and eloquent tissues in the patient, which necessitates an elaborate segmentation stage from MRI data under various guises, namely angiographic data and diffusion tensor imaging for vessels and nerves, respectively, and functional imaging for eloquent portions of the brain.

Nonholonomic Model

Webster et al[14] developed a nonholonomic model of the kinematics of a beveled tip needle, which is analogous to a bicycle with locked steering, consistent with the assumption that this needle follows a deterministic trajectory upon insertion into tissue. According to this model, the needle tip moves forward along a prescribed curved trajectory. While the wheels do not move sideways, the bicycle can achieve any intended pose within the plane. The inputs to this nonholonomic model are insertion velocity u_1 and rotation velocity u_2, as depicted in Figure 4. As alluded to in the Tip-based Steering section, the bicycle model

simplifies to a unicycle by neglecting the front wheel coordinate frame.

As shown in Figure 4, frames B and C are coupled rigidly to each other, while the origin of C is separated by distance l_1 from frame B, along its z axis. The y-z plane of the frame C is rotated about the x-axis by angle ϕ. The kinematic model is the following:

$$\begin{cases} \dot{g}_{AB}(t) = g_{AB}(t)\left(u_1\hat{V}_1 + u_2\hat{V}_2\right) \\ n(t) = R_{AB}(t)l_2e_3 + p_{AB}(t) \end{cases} \qquad (8)$$

where g_{AB} and R_{AB} denote the rigid-body transformation as well as the rotation matrices between frames A and B; u_1 and u_2 are velocities of insertion and rotation. In addition, $\hat{V}_1$ and $\hat{V}_2$ refer to pure needle insertion and shaft rotation, respectively; p_{AB} is the position of frame A in relation to B; e_3 is specified by the relation $p_{BC} = l_1e_3$, where p_{BC} is the position of frame B relative to C, and lengths l_1 and l_2 are also as depicted in Figure 4. This model is further simplified based on a unicycle, using Lie algebra:[24]

$$\xi(t) = \left(g^{-1}(t)\dot{g}(t)\right)^{\vee} = \begin{bmatrix} \kappa u_1(t) & 0 & u_2(t) & 0 & 0 & u_1(t) \end{bmatrix}^T \qquad (9)$$

where $g(t)$ is the member of the rigid-body Special Euclidean group known as *SE(3)* and ξ is the corresponding component *se(3)* of the Lie algebra associated with *SE(3)*. The function $g(t)$ denotes the 6-degree of freedom pose expressing the position and orientation of the frame of the needle tip in 3D space, while $\xi(t)\epsilon\mathbb{R}^6$ is the 6-vector comprised of the frame's linear and rotational velocities. The

input parameters u_1 and u_2 represent the needle's velocities of rotation and insertion, respectively, while κ denotes the curvature of central axis of the needle inserted into tissue. As described by De Luca and Oriolo,[25] an advantage of non-holonomic behavior in robotics is that the mechanism can be completely controlled with a reduced number of actuators. On the negative side of the ledger, planning and control are more complex than that of holonomic systems, which pre-supposes special control techniques.

Beam Models

Glozman's flexible needle model represented the interaction between the inserted needle and the penetrated tissue as an aggregation of virtual, distributed springs,[21] as depicted in Figure 8, which could be linearized and formalized as a collection of forces $F_i = k_i(w_i - w_{0i})$, where k_i is the spring constant, w_i is position after deformation at spring point i, while w_{0i} is the undeformed position of point i. Assuming that these forces are proportional to the deflection, the deflected shape of the needle cannot be estimated on the basis of a single-element needle model, but rather necessitates a discretization into a finite collection of beam elements, where each element is subject to two neighboring forces applied at its end-points. The deformation of the needle is thus expressed as a function

$$y(x) = N_1\phi_1 + N_2\phi_2 + N_3\phi_3 + N_4\phi_4 \qquad (10)$$

where N_1, N_3 designated the coordinates and N_2, N_4 the slopes at $x = 0$ and $x = l$ of each beam element, respectively, and where ϕ_i denoted shape functions of third degree, suitable for a finite elements (FE) solution. A typical beam element-based FE matrix system was proposed as a result:

$$KN = Q \qquad (11)$$

where matrix K is the set of coefficients of $N_{i,j}$ of translation and slope DOFs, N is the aggregate of nodes $N_{i,j}$,
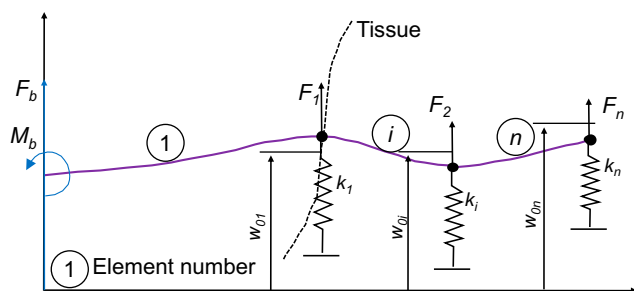

Figure 8 Glozman's beam element and spring model for needle insertion into tissue. Data from DiMaio and Salcudean.[20]

subscript i denotes the element index while j is the DOF of element i, and finally Q represents a combination of stiff-ness coefficients and initial positions of the nodes at the times of their penetration with the needle w_{0i}. Assuming we have the translation and the rotation of the needle base, expression (10) enables the calculation of the translation-rotation 3-DOF vector of the needle tip, based on forward kinematics. Conversely, needle insertion equates with a need to reach the target with the tip while avoiding possible obstacles. As a result, a particular trajectory is prescribed for the needle tip, whereby the required base manipulation can be calculated, which in turn is restated as an inverse kinematics problem: for a prescribed trajectory of position and orientation of the tip, one can determine the required translation and orientation over time or in tissue coordinates of the needle base. The use of spring models to compute local deformations leads to a fast plan-ning algorithm in relation to pure FE-based methods such as DiMaio's, cited earlier.

Related models were produced by Abolhassani et al,[26–28] in conjunction with robotic prostate therapy. In[27] this group modeled the infinitesimal force, as a function of unit tissue displacement K_e, needed to update the insertion profile of the needle, based on the formula:

$$K_e = \frac{\sum_{j=i-n+1}^{i}\left(\frac{f_j - f_{j-1}}{x_j - x_{j-1}}\right)}{n} \qquad (12)$$

where f_j and x_j respectively model force in the direction of insertion as well as tissue indentation at the jth time step, parameter i denotes the time step index of the force peak at the point of tissue puncture, and n represents the time count prior to puncture. In[28] Abolhassani updated the needle deflection, based on a cantilever with spring sup-port. Finally,[26] proposed the following model for bevel-tip needle deflection:

$$v = \sum_{i=0}^{n}\left(3\Delta M_{ri}L^2 - \Delta F_{ri}L^3\right)/6EI \qquad (13)$$

where the left-side value v is the tip deflection; n denotes the time count; ΔM_{ri} and ΔF_{ri} represent moment and force variations between consecutive time steps. Finally, the right-side elements E and I denote the needle's Young's modulus as well as its moment of inertia.

Stochastic Models

The motivation for a stochastic needle-steering model stems from the inherent variation in motion over successive inser-tions. In the absence of such variability, an exact solution could simply be obtained by integrating a differential

expression such as the unicycle model in (9). In contrast, repeated insertions of a needle tend to produce a series of slightly different paths, which supports a stochastic model where noise is added to deterministic components. Park's model imbeds this stochastic aspect based on noise terms for the linear and angular velocities v and ω (denoted u_1 and u_2 in preceding text):[24]

$$\omega(t) = \omega_0(t) + \lambda_1 w_1(t) \text{ and } v(t) = v_0(t) + \lambda_2 w_2(t) \quad (14)$$

where $\omega_0(t)$ and $v_0(t)$ denote ideal, uncorrupted inputs, $w_1(t)$ and $w_2(t)$ represent Gaussian white noise functions, and the parameters λ_1 and λ_2 are weighting factors. This consideration leads to an updated unicycle model, described in the following expression:

$$\left(g^{-1}(t)\dot{g}(t)\right)^{\vee} dt = \begin{bmatrix} \kappa v_0(t) & 0 & \omega_0(t) & 0 & 0 & v_0(t) \end{bmatrix}^T dt \\ + \begin{bmatrix} 0 & 0 & \lambda_1 & 0 & 0 & 0 \\ \kappa\lambda_2 & 0 & 0 & 0 & 0 & \lambda_2 \end{bmatrix}^T \begin{bmatrix} dW_1 \\ dW_2 \end{bmatrix} \theta$$

(15)

where $dW_i = W_i(t + dt) - W_i(t) = w_1(t)dt$ are incremental variations of corresponding Wiener processes $W_i(t)$. This stochastic model represents a differential equation on the Special Euclidean group $SE(3)$.

Path Planning and Robotic Systems

Several groups have proposed robotic assistants for needle-based intervention, in a manner that may have implications for neurosurgical procedures. As depicted in Figure 2, there is typically an imaging component, which may be leveraged within image-guided navigation, where robotic fiducials akin to the Z-bars of Figure 13 (see the upcoming section on Clinical Applications of Needle-based Therapies) can be used to establish the image-to-patient/robot space transformation. Moreover, many have formulated strategies specifically for dealing with position uncertainty and intraoperative motion in needle-based therapy delivery.

Stochastic Planning: Factoring Uncertainty

Alterovitz et al have developed needle path planning techniques that model uncertainty of the needle motion to improve the likelihood of attaining the target successfully while circumventing obstacles.[29,30] This framework, aptly named Stochastic Motion Roadmap (SMR), formulates needle path planning in terms of a Markovian Decision Process (MDP) and strives to achieve the best probability of success with Dynamic Programming (DP). This approach represents motion in terms of a formal state space, which leads to a roadmap that makes explicit the trajectory uncertainty of

the tissue configuration, while formulating the path plan as an MDP. It finally arrives at a solution via DP that maximizes the probability of a successful outcome. The SMR framework enabled the computation of actionable needle paths in conjunction with 2D tissue models. Modeling uncertainty in this manner resulted in needle motion plans starkly different compared to traditional shortest paths, with an emphasis on somewhat lengthier paths with increased clearance in relation to obstacles, to maximize the likelihood of a successful outcome.

Coping with Soft-Tissue Motion Through Intraoperative Imaging

In many cases, due to either a large amplitude of intraoperative soft tissue motion or a tight accuracy requirement in relation to the amplitude of such motion, the imaging component features both preoperative imaging-based planning and intraoperative imaging-based updates to the anatomical model, which is typically true of neurosurgery. To best cope with intraoperative soft tissue motion, some robotic systems are designed to be explicitly compatible with intraoperative imaging. For minimally invasive neurosurgery that proceeds through a burr-hole, this requirement entails intraoperative CT or MRI. Assuming that ionizing radiation dose is a consideration, which suggests MRI instead of CT, the reliance on intraoperative imaging-based model updates in turn means that the needle and the robotic delivery system must be non-ferrous and in general MRI-compatible. MRI-compatibility has been an important theme in neurosurgical robotics,[31,32] including the NeuroArm, developed by Sutherland and his colleagues at University of Calgary,[33] and sold by IMRIS Inc. (Winnipeg, Canada) as depicted in Figure 9A.[34]

Meanwhile, G.S. Fischer and his colleagues at Worcester Polytechnic Institute have been developing a MRI-compatible robotic assistant for deep brain stimulation, in collaboration with Albany neurosurgeon J.G. Pilitsis, as shown in Figure 9B.[35] The workspace of the robot, which is essentially an articulated plastic assembly, is designed to fit around the head of the patient and within the tight confines of the bore of an MRI scanner. The design features non-ferrous metals and magnetic field-tolerant circuitry within an electromagnetic interference-shielded enclosure.[35]

In conjunction with this MRI-compatible DBS robotic assistant, the first author has sought to develop a deformable multi-surface model of a digital deep brain atlas,[36] which is conducive to fast updates in conjunction with intraoperative MR imaging.[37] The efficiency of the MRI reconstruction itself must also be an important consideration. Huang et al
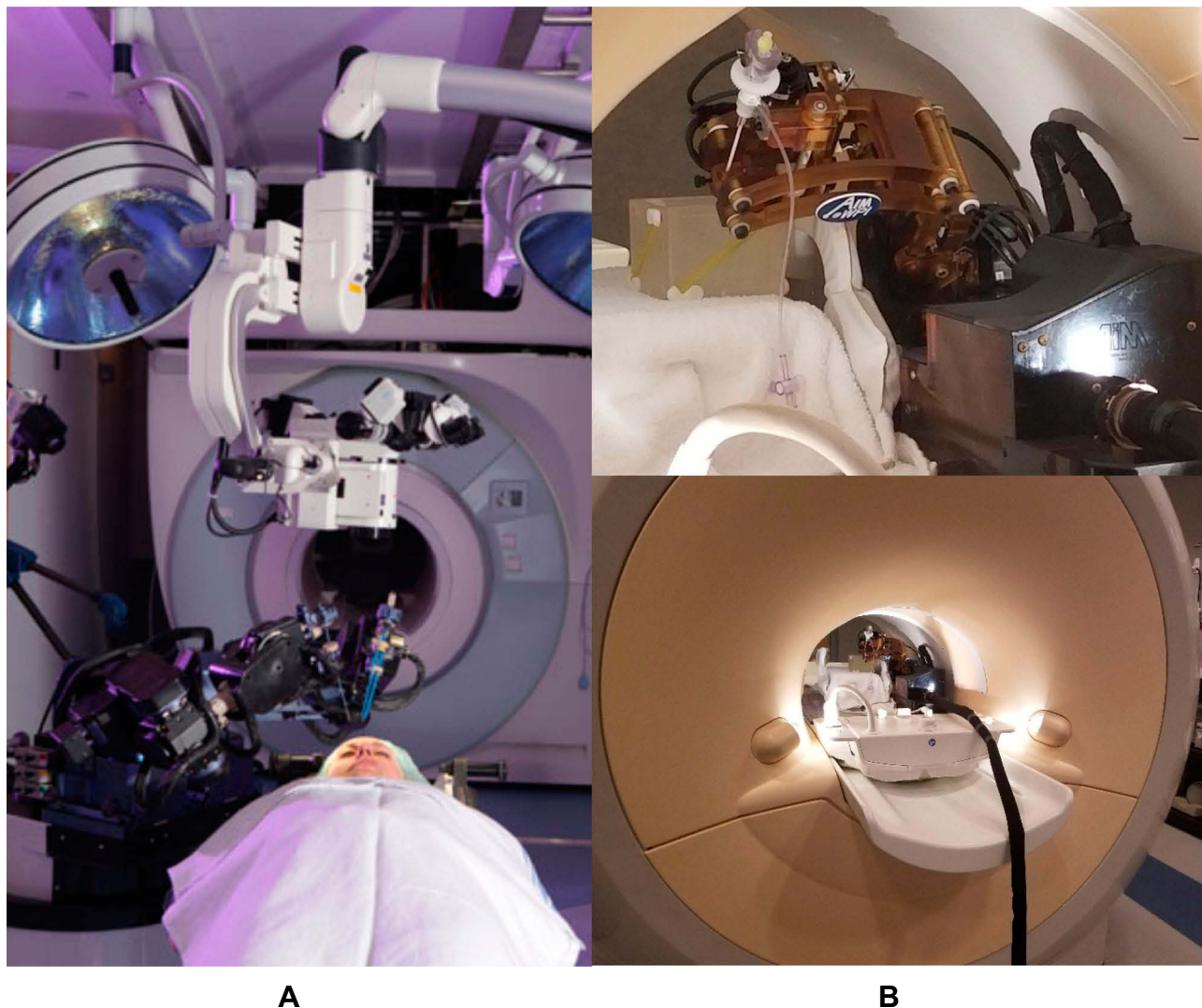
Figure 9 MRI-compatible neurosurgical robotics. (**A**) NeuroArm MRI-compatible neurosurgery robot, shown with patient in foreground and MRI scanner in the background. Reproduced with permission from NeuroArm. Project.[34] (**B**) Development of MRI-compatible deep brain stimulation robotic assistant by G.S. Fischer et al[35] Unpublished DBS robot images graciously contributed by G.S. Fischer of Worcester Polytechnic Institute.

have proposed fast reconstruction of multi-contrast MR images from partially sampled signals in k-space.[38] Multi-contrast MRI can lead to highly discriminating MR images of basal ganglia, such as the subthalamic nucleus, whose local contrast based on differences in iron content leads to structure-wise variations in T_2 relaxation times.[39,40] Huang's MRI reconstruction method exploits simultaneous multi-contrast reconstruction as the combined minimization of three terms. These terms correspond to i) a least-squares fitting residual between the Fourier transform samples and k-space measurements, ii) a first regularization term based on joint total-variation of the reconstructed MR image, and iii) a second regularization term favoring small wavelet basis coefficients of the reconstructed MRI signal.

Exploiting Simulations to Anticipate Pitfalls

Computer simulations can be used to ask and answer what-if questions, which relate to patient-specific tissue deformations; these simulations result in descriptive pre-operative planning that allow surgeons to anticipate pitfalls while optimizing paths for needle insertion. This area can be envisioned as an extension of the concept of uncertainty in determining an ideal path that may not be the shortest but is optimal in offering a margin of error in circumnavigating critical or eloquent tissues of the brain. These simulations typically center on coupling between finite elements models of both the steerable needle and deformable tissue. Finite elements are based on a restatement of the Principle of Virtual Work in a weak form, which leads

to a conversion of an integrable continuum mechanics problem into a matrix problem solvable by linear algebra. These simulations also require a model of the patient anatomy, which entails either structured hexahedral mesh or unstructured tetrahedral mesh. While the needle model is inserted, the simulations represent forces that characterize needle-tissue friction and tissue cutting, as well as shape changes to both the needle and the tissue. Traditional finite elements may require dynamic remeshing to ensure that the mesh conforms to the simulated needle path as well as enforce high-quality elements. Meshless mechanics obviate this remeshing requirement at the cost of a significant computational effort. Contributors in the FEM area of needle insertion modeling area include Alterovitz and Chentanez et al, who authored papers on 2D and 3D simulation, respectively.[41,42]

Bui et al developed a dynamic remeshing approach that increases the resolution near the penetrating needle in real-time.[43] The unique feature of,[43] which is encountered nowhere else in the literature, to our knowledge, is its simple but accurate a posteriori error estimation approach, which guides the local refinement of the mesh through robust mathematical arguments. Combined with the ability to describe the boundary of the needle and of the organ implicitly (without a conforming finite element mesh), error estimation makes the method a robust and accurate candidate for simulating topological changes and needle insertion in real time. Bui's work exploits a series of real-time simulation approaches founded on advanced finite elements using CPUs and GPUs, thereby enabling "Real-time error control for surgical simulation",[44] "Real-time simulation of contact and cutting of heterogeneous soft-tissues"[45] and "Real-time Patient-Specific Needle Insertion Simulation using Corotational Cut Finite Elements".[46] The latter work is depicted in Figure 10. Recent work by Ju addressed meshless mechanics-based simulation of a bevel-tip needle insertion.[47]

Despite the afformentioned simulation advances, numerical discretization and discretization error control are but two of the steps involved in numerical simulation in surgery. The most challenging steps are to define the proper physical model governing the interaction of the tool with the tissue, given limited experimental information, and measure the modelling error, as depicted in Figure 11. Once the simplest and most representative model has been identified, e.g. using Bayesian inference,[48] material parameters can be estimated. If the information available is sparse and scarce, a Bayesian approach may be particularly suitable,[49,50] which can also be applied to anisotropic and inhomogeneous materials.[51] Recently, advanced methods used in uncertainty quantification have been extended to estimate the relative importance of parameters appearing in hyperelastic constitutive models used in surgical simulation, e.g.[52–54]

Clinical Applications of Needle-Based Therapies

To better inform the reader on the revolution underway in neurosurgery that is founded on both needle-based minimally
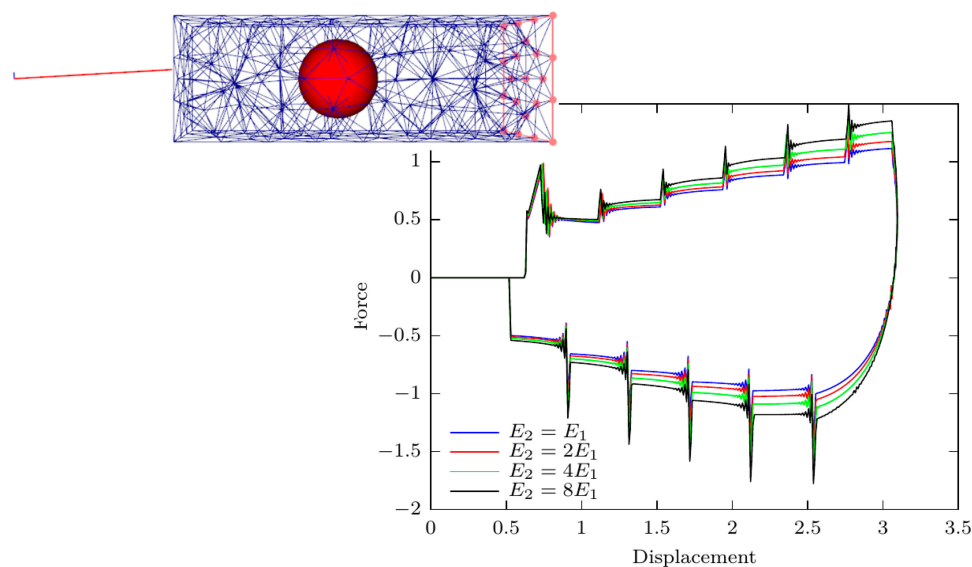

Figure 10 Plots of force against displacement, demonstrating the effect of the variation of the ratio of Young's moduli E2/E1, for simulated needle insertion into simulated soft tissue. Image courtesey of S.P.A. Bordas.
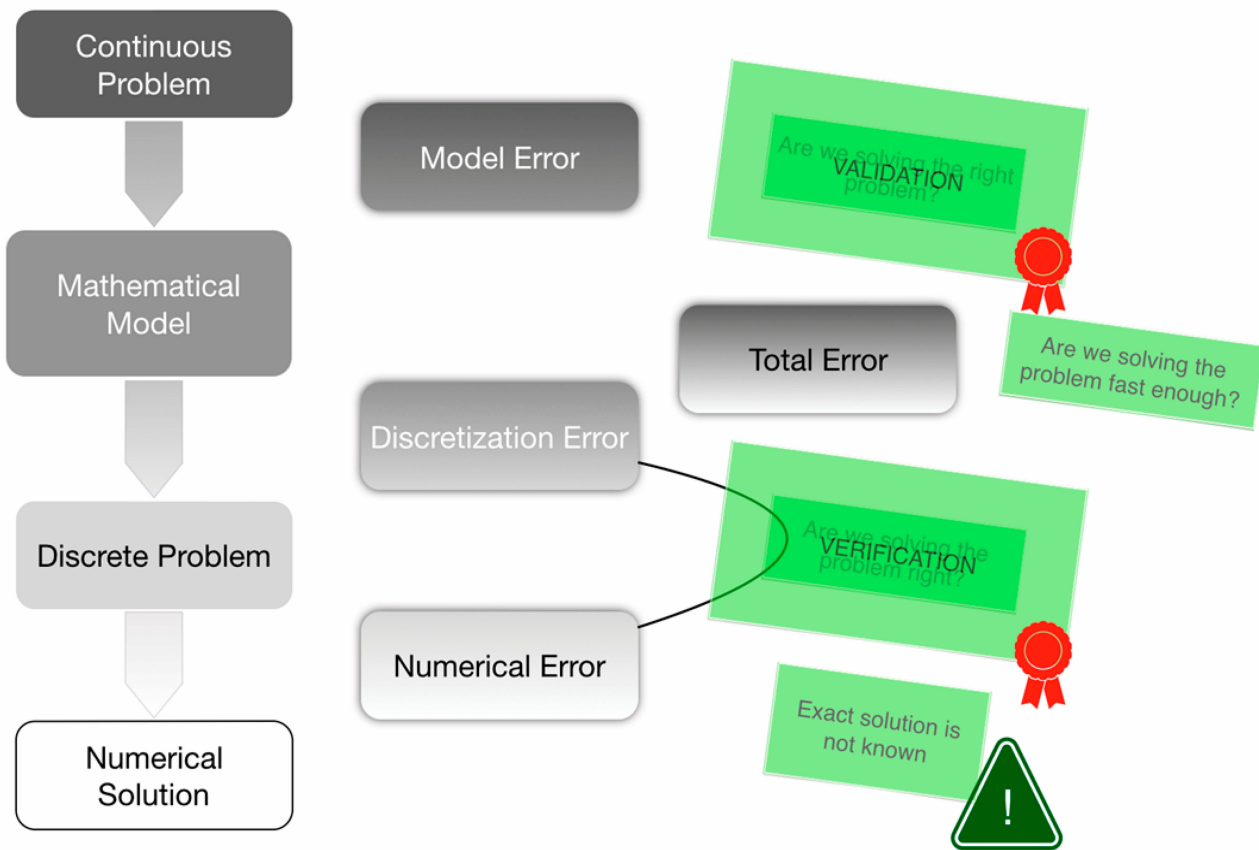
Figure 11 Mathematical modelling process and its pitfalls, with some solutions provided by Validation (Are we solving the right problem?) and Verification (Are we solving the problem right?), which elicits other questions about efficiency and whether an exact solution exists.

invasive therapies and robotic assistance, it is vital for us to paint a broad picture of the clinical areas of application. To fulfill this objective, the following section surveys deep brain stimulation, SEEG, drug delivery in the brain, neurological aspiration, brachytherapy as well as thermal ablation, while describing the relevant neuroanatomy. It is also important for the reader to consider this section not merely as an overview of robotic needle-steering applications in the literature, but rather a broader overview of neurosurgical needle-based therapies, which could broadly benefit from robotic targeting and therapy delivery. In other words, this survey does not just serve as a digest of existing technologies, but a connect-the-dots exercise that could elicit some what-if questions in interested readers.

Stereotactic Needle-Based Brain Biopsy

A brain biopsy consists of the surgical extraction of a relevant tissue sample needed for a pathological diagnosis that will be the basis for subsequent treatment, including resection surgery, chemotherapy or radiation therapy.[55] The justification for stereotactic needle-based

biopsy instead of an open-cranium procedure is to minimize adverse effects while still achieving high diagnostic accuracy. In the past two decades, medical imaging techniques have been integrated into neuro-oncology to enable the visualization of the location and morphology of brain lesions.[56] However, their relevance to histopathology is limited, given that physiological imaging techniques such as PET, SPECT, or MR spectroscopy have yet to fully replace biopsy-based histopathological diagnosis of unknown lesions.[56] As Tilgner notes,

> Even if a glial tumor is suspected, an oligodendroglioma cannot be distinguished from an astrocytoma using neuroimaging techniques. Therefore, a patient may not be entered in a chemotherapy protocol without a histopathological or molecular genetic analysis.[56]

Tissue diagnosis remains the mainstay requirement of oncologic treatment and is likely to remain so for the foreseeable future.

Stereotactic techniques for needle-based biopsy mirror the evolution of stereotactic neurosurgery, with frame-

based interventions preceding frameless stereotaxy. Early attempts at stereotaxy date back to Zernov in 1889 and to Horsley 1906.[55] Zernov invented an apparatus that was fastened to the head of the patient and exploited for determining landmark points that could anchor a registration with a map of cranial structures. He exploited this head-frame to treat a brain abscess. Unaware of Zernov's stereotactic frames, Horsley proposed a method of locating cerebral anatomy in animals based on a construction endowed with a 3D coordinate system, thereby inventing the word stereotaxy based on the Greek roots stereo: "three-dimensional" and taxis: "to move toward". Despite this progress, neuroanatomical structures below the cortex could not be reliably tracked until intracranial imaging was available, coinciding with the introduction in 1947 of the first human stereotactic system by Spiegel and Wycis, the encephalotome,[55] soon followed by Leksell's stereotactic frame in 1949.[57] The development of frame-based registration and the advent of tomographic imaging, in the form of CT in 1973 and MRI in the early 1980s, led to other neurosurgical guidance.[58,59] These frames were first used to lesion specific neural structures to treat movement disorders and epilepsy, but they soon were applied to the biopsy of tumors.[55]

As described by Olivi,[55] and depicted in Figure 12, the justification for a minimally invasive, stereotactic approach to biopsy over a traditional craniotomy-based procedure is that stereotactic procedures maximize accuracy of the diagnosis while minimizing surgical risks. This accuracy is vital for optimizing adjuvant treatments founded on knowledge of tumor histology. Typical scenarios that motivate a stereotactic biopsy include the following: i) lesions untreatable by surgical excision or bereft of symptomatic mass effect; ii) lesions in eloquent cortical regions or deep sub-cortical structures, where open resection comes with an unacceptable risk of morbidity or mortality; and iii) infiltrative lesions without a clear brain-tumor margin, such as gliomatosis cerebri, the excision of which may be coupled with a significant loss of normal brain tissue. Moreover, if the appearance in MRI of the lesion or the disease progression suggest an alternative explanation, such as an infection, a stereotactic approach is deemed preferable to a traditional open-cranium surgery.[55] Contraindications also include highly vascularized tumors, which should not be treated
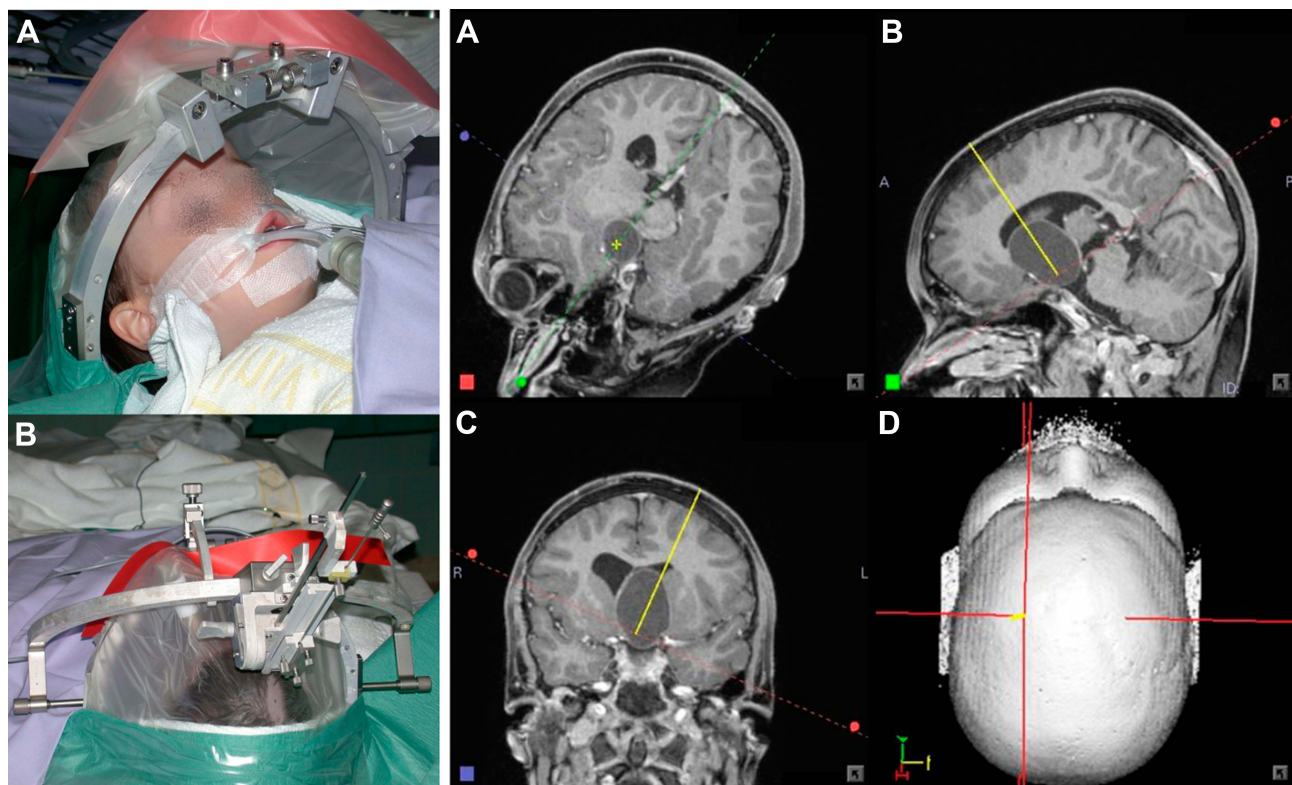

Figure 12 Stereotactic needle-based biopsy of large craniopharyngioma cyst in 11-year-old boy. (i) Operating room setup. (**A**) Anesthetized patient with stereotactic ring affixed to his head prior to the procedure. (**B**) Probe oriented towards the surgical entry point. (ii) (**A**–**D**) Surgical planning and navigation for biopsy. The procedure involves puncturing and draining the cyst, based on a visualization oriented according to the needle trajectory. Copyright © 2012. Reproduced from Trippel M, Nikkhah G. Stereotactic neurosurgical treatment options for craniopharyngioma. *Front Endocrinol (Lausanne)*. 2012;3:63.[61]

stereotactically because of the relatively high risk for hemorrhage.[60]

Frame-based neurosurgical navigation emphasizes four geometries: arc-radius, polar coordinates, focal point, and phantom targeting. Polar coordinates navigation represents frame-based guidance of the surgical probe angles in relation to a skull entry point. Typically, two angles in mutually orthogonal planes are combined to characterize a unique trajectory; additionally, the depth of the insertion specifies the remaining degree of freedom. The arc-radius, exhibited by the Leksell frame, is a subtle variation on this theme: its guidance exploits a geometry whereby a probe should align with the center of a semicircular arc if inserted perpendicularly from any point along the arc. Adjustments in relation to this preoperative scanning, without the arc in place, and to this assumption enable targeting within the cranium and typically require a computation that converts from Cartesian to polar coordinates. If CT is used, the frame is secured to the head of the patient and remains fixated until the procedure. At the beginning of the procedure, the arc is installed and manipulated to enable fine anterior-posterior and vertical adjustments to the arc center.

In both frame-based and frameless systems, the rigid transformation is defined between image space, based on either type of landmarks visible in the preoperative CT or MR image, and patient space defined in the operating room. The frame-based approach exploits graduated bars that form a cube as well as N-shaped fiducial bars on each side of the frame, with a salient diagonal bar that connects opposite corners on each side, as shown in Figure 13. These bars are easily visible in tomographic images, where in particular the intersection of the diagonal with each xy image plane provides information about the longitudinal z-coordinate.[62] Each elliptical intersection is located automatically by image analysis, which enables fully automatic 3D methods for registering the preoperative volumetric image with the physical frame. For frameless systems, a rigid registration is achieved through homologous point pairs, localized at surgical fiducials glued onto the scalp or inserted into the cranium, whose resulting transformation is possibly refined based on surface registration. In the frameless case, the patient-space points are localized through divots embedded into the fiducials, using a stereotactic probe that is optically tracked in real-time, in conjunction with a system manufactured commercially such as by BrainLab or Medtronic.[63,64] Quantitative studies of frameless stereotactic localization determined
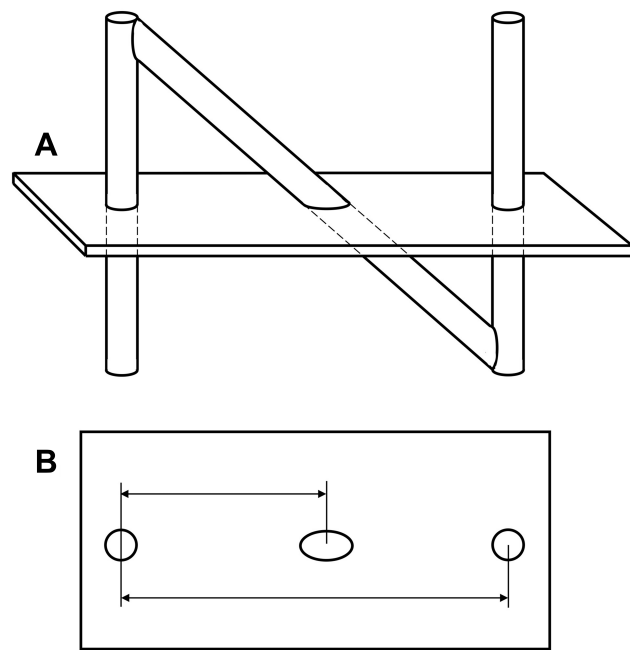

Figure 13 N-shaped fiducials for frame localization within a medical image. (**A**) Lateral view of the N-fiducial. Each N-fiducial result in a characteristic intersection with every image plane. (**B**) Typical intersection of the fiducial with a CT image. This intersection with the fiducial results in a pair of circles and an ellipse. The location of the ellipse between the two circles is a function of the height at which the tomographic image plane intersects the diagonal rod. Copyright © 2006. Wikipedia. Reproduced from uploader. Stereotactic surgery. Available from: https://en.wikipedia.org/wiki/Stereotactic_surgery.[66]

that their accuracy is comparable with frame-based methods, which were considered as the prevailing standard for stereotactic neurosurgery.[65]

The main complication associated with stereotactic biopsy is hemorrhage resulting from iatrogenic damage to the cerebrovasculature in the surgical corridor of the needle or at the biopsy site itself. Navigation systems with a suitable view enable trajectory planning to avoid crossing sulcal and pial surfaces and to avoid blood vessels. In addition, pathologically friable vessels present in the tumor can also lead to hemorrhagic complications. Kongkhan et al reported complications rates for stereotactic biopsy based on 622 cases: 6.9% morbidity, 1.3% mortality, 2.9% transient neurological deficit, and 1.5% permanent neurological deficit.[67] Moreover, they found that deep-seated lesions were associated with increased complications. However, these risks are likely to be substantially lower than the risks that would be imposed by open excisional biopsy of these high-risk or deep-seated brain lesions.

Deep Brain Stimulation

As depicted in Figure 14, deep brain stimulation (DBS) is an electrical treatment for neurodisorders such as Parkinson's disease (PD), Alzheimer's disease (AD), and epilepsy, which
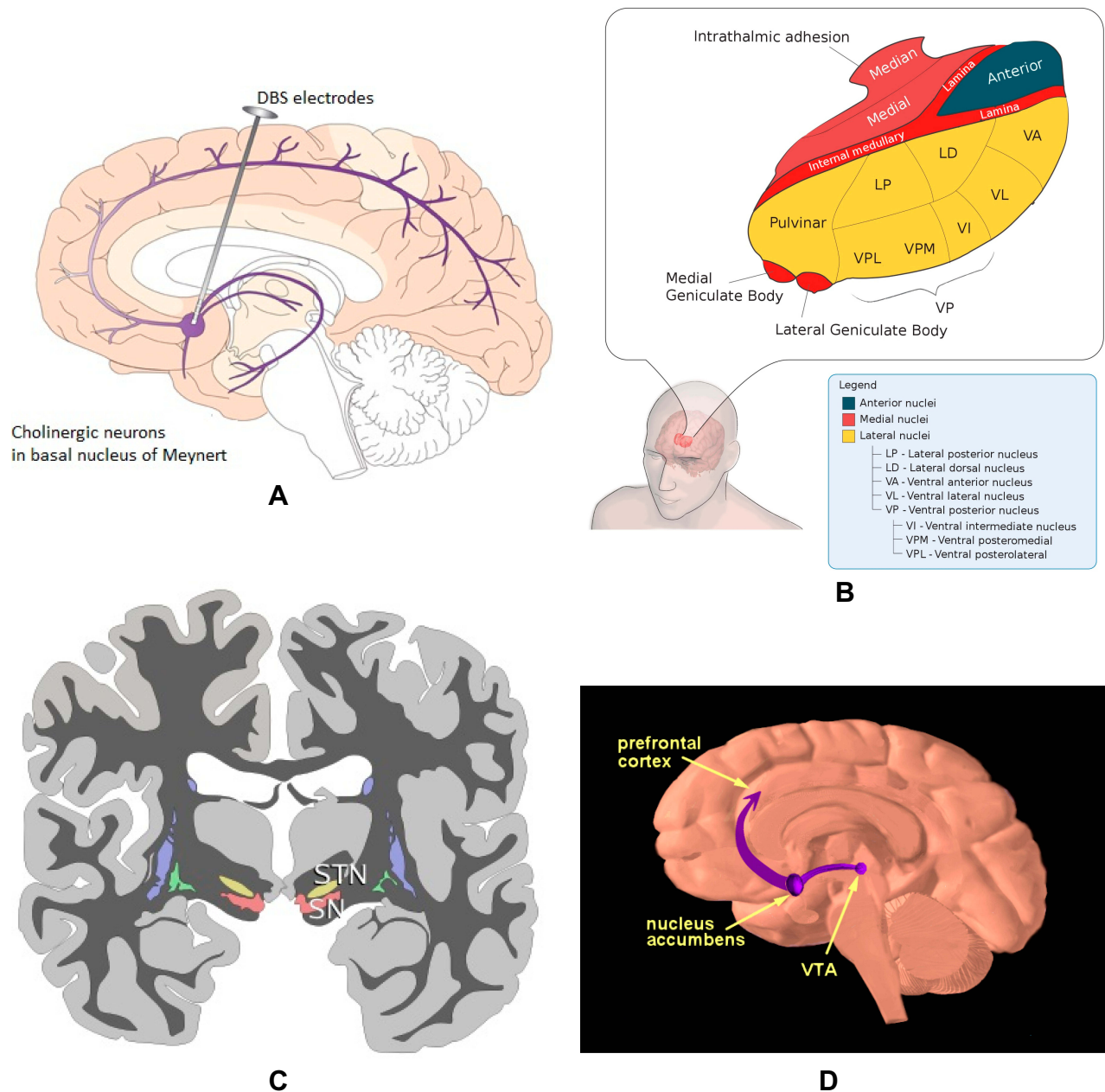
Figure 14 DBS neuroanatomical targets. (**A**) Nucleus basalis (NB) targeted in Alzheimer's disease and in Lewy body disease. Copyright © 2015. Reproduced with permission from Zhang Q, Kim Y-C and Narayanan NS. Disease-modifying therapeutic directions for Lewy-Body dementias. *Front. Neurosci*. 2015;9:293.[73] (**B**) Thalamus, the anterior nucleus of which is shown in dark blue and targeted for DBS of epilepsy. Copyright © 2011. Wikipedia. Reproduced from uploader. Thalamus-schematic-de.svg. Available from: https://commons.wikimedia.org/wiki/File:Thalamus-schematic-de.svg.[74] (**C**) Subthalamic nucleus (STN) and substantia nigra (SN) depicted in coronal plane in yellow and red, respectively.[75] (**D**) The reward pathway spans several parts of the brain, as highlighted: the ventral tegmentum (labeled VT), nucleus accumbens, as well as the prefrontal cortex. Reproduced with permission. National Institute on Drug Abuse. Public Domain Picture: Brain reward pathway. Available from http://www.publicdomainfiles.com/show_file.php?id=13989816622720.[76]

is also considered feasible for obsessive-compulsive disorders (OCD) and treatment-resistant depression (TRD).[1] The subthalamic nucleus is the target commonly used for PD, while the nucleus basalis, anterior nucleus of the thalamus, subgenual cingulate (not shown), and nucleus accumbens are, respectively, targeted for AD, epilepsy, TRD and OCD.

In the traditional DBS framework, a preoperative MRI scan of the head of the patient is acquired, a stereotactic frame is fastened to it, which is then imaged with a CT scan, and the trajectory of the electrode-carrying needle is established based on the co-registered MRI and CT images and a printed atlas of basal ganglia. This traditional technique

restricts the choice of approach of the surgeon and requires significant mental reconstruction by the neurosurgeon.[68] It may also involve intra-operative microelectrode recordings (MER), which can result in longer operating times and a higher risk of complications.[69] In contrast, computerized DBS practice relies on a digital atlas of deep brain structures,[36,70] nonrigidly registered to the preoperative T_1 or T_2-weighted MRI scan of the patient. In addition to image guidance, McIntyre and his collaborators have also advocated the consideration of patient-specific DBS simulations, which exploit a tractographic brain model based on MR Diffusion Tensor Imaging (DTI) to enable targeting that fully leverages brain connectivity.[71,72]

Stereoelectroencephalography

Stereoelectroencephalography is a technique for localizing epilepsy through the strategic placement of multiple depth electrodes, as depicted in Figure 15.[77,78] SEEG competes with a subdural exploration (SDE) approach, the placement of recording electrodes on the surface of the brain, in the manner that it models partial epilepsies as a distributed three-dimensional network, as opposed to a local pathology that radiates outward, and in its sparse sampling approach as opposed to continuous over adjacent brain areas.[78] Modern neuroimaging techniques and digital video-EEG enable a precise localization of the epileptic network.[77] The main distinction between SEEG and SDE is the truly
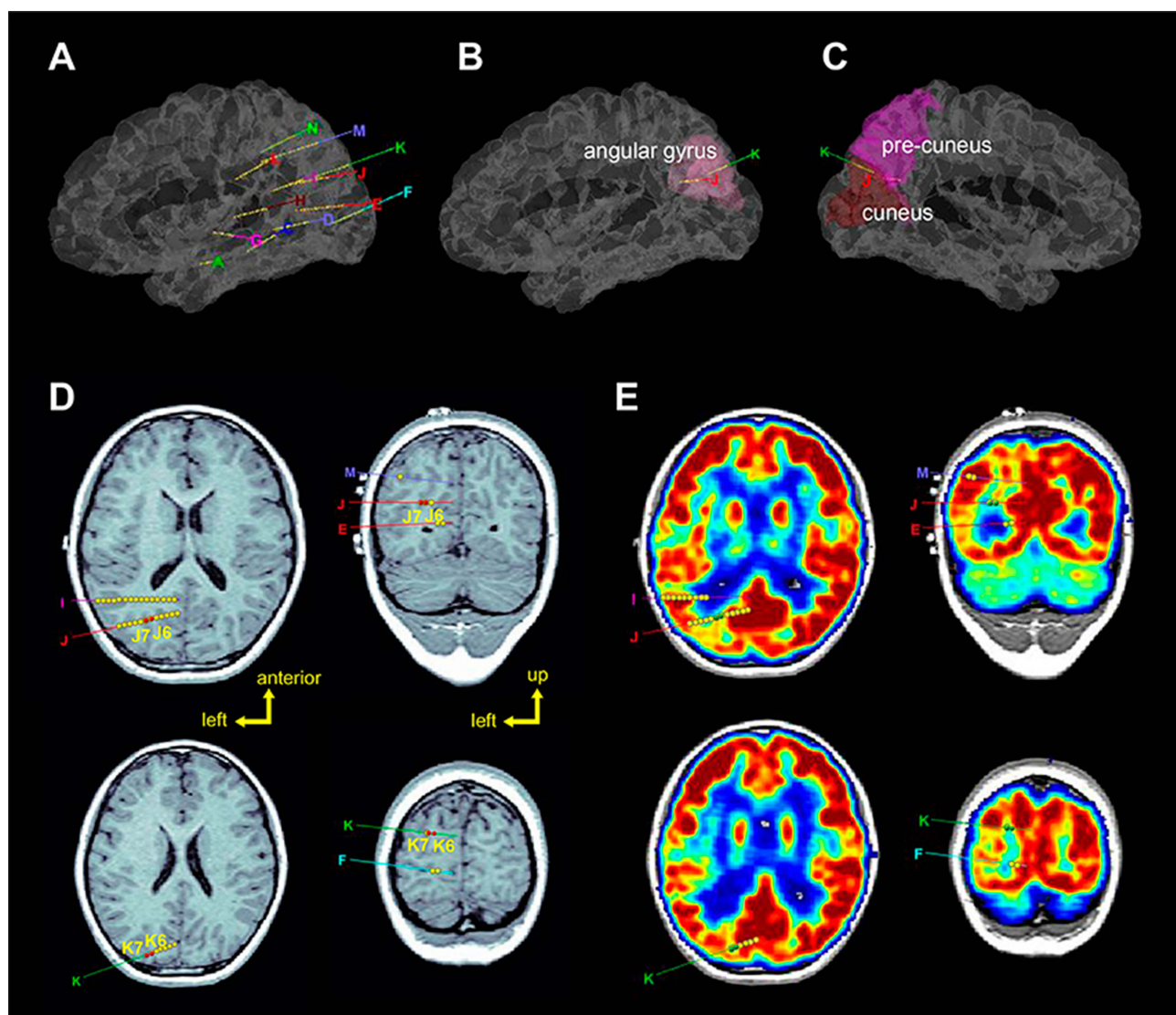

Figure 15 SEEG surgery planning. (**A, B, C**) 3D volume renderings of patient brains, with overlaid labels of electrode locations defined in stereotactic space. (**D**) Axial and coronal planar representations of patient T1-weighted brain image, with electrode paths J and K highlighted. Epileptogenic zones are labeled as J6, J7, K6, and K7. (**D**) Comparable axial and coronal planes of a co-registered PET volume: green labels correspond to lesser metabolic areas. Copyright © 2018. Reproduced with permission from Wang J, Wang Q, Wang M, et al. Occipital lobe epilepsy with ictal fear: evidence from a stereo-electroencephalography (sEEG) case. *Front Neurol.* 2018;9:644.[77]

dispersed sampling of SEEG that extends to deep locations in the cortex that are unreachable by SDE.[77] Based on the advantage in precise localization, some clinical applications support SEEG over SDE. SEEG can cover both hemispheres and basal ganglia extensively through broadly based sampling. Enabling technologies include MRI and 3D angiography, descriptive surgery planning founded on multimodal imaging, and robotic positioning of electrodes. In addition, SEEG requires only small holes in the skull for needle-guided electrode implantation, while SDE requires a large craniotomy and entails substantially higher risk of morbidity to the patient.

SEEG electrode positioning is motivated by the notion of an epileptic "network", or EN, founded on a functional correlation between a collection of anatomical sites. This network denotes the portion of neuroanatomy close to a putative epileptogenic zone (EZ). Beyond this local circuitry, the EN includes neural sites remote and sometimes contralateral to the EZ. Typically, an SEEG acquisition fulfills four aims:[79] it (1) pinpoints the EZ and core areas of the EN, (2) identifies the broadly distributed portions of the EN, (3) localizes elements of the eloquent cortex near the EN, and (4) identifies unaffected portions of the brain. Gonzales-Martinez published a study of 101 cases of robotically assisted implantation of SEEG electrodes.[80] Surgery planning took 30 mins on average, and the procedure itself required 130 mins on average. Accuracy statistics of robotic SEEG consisted of median values of entry point error and target point error of 1.2 mm and 1.7 mm, respectively.

Intracerebral Drug Delivery

Several neurodisorders are characterized by localized lesions in brain tissue, including traumatic brain injury, stroke, tumors, epilepsy, and neurodegenerative disorders. To treat these localized pathologies, a new technique is emerging that exploits the direct delivery of therapeutic agents to the afflicted site, designated as compartmental or local therapy. Potentiated by omnipresent surgical navigation as well as advances in medical imaging and in minimally invasive techniques, this approach exploits molecular therapies that modulate physiological functions while exhibiting high cellular specificity and while exploiting accurate spatial and temporal targeting.[78]

As shown in Figure 16, Dagdeviren proposed a Miniaturized Neural Drug Delivery System (MiNDS), with a diameter of 200 μm, which exploited an integrated tungsten electrode of 75 μm for recording neural activity. This signal was acquired to provide feedback at both multiple neuronal scales.[78] This device imbeds two fluidic channels, made of borosilicate, characterized by inner and outer diameters of 20 and 30 μm. It is connected to wireless pumps for supplying fluidic therapy. The MiNDS device was validated through rat brain PET studies to track drug infusions in deep brain structures, subsequent to phantom trials. Specifically, an S-MiNDS device was implanted in a rat, targeting the substantia nigra (SN). This rat study validated the selective infusion capacity of the MiNDS device, through infusions of different sizes of copper-64 (Cu-64), an isotope commonly used in PET scans. In a similar vein, Engh described a cerebral therapy delivery system based on variable duty-cycle spinning of hollow beveled needles, which were validated through cadaveric trials.[3]

Likewise, convection-enhanced delivery (CED) exploits cannulas in combination with an infusion process in order to deliver targeted toxins to tumors.[81,82] These drugs typically correspond to molecules too large to traverse the blood-brain barrier and that must be transported by CED into the brain. The CED infusion increases drug efficacy while reducing side effects to healthy brain tissue and the rest of the body. Like other needle-based therapies, CED involves drilling a burr hole in the patient's skull to insert a cannula that extends to the tumor. Several cannulas may be placed to reach the tumor from different angles, depending on its size and geometry. The drug in liquid form is pumped through the cannula and ultimately infused into the tumor tissue.[82]

Stereotactic Needle-Based Aspiration

In addition to the above, hollow needles can treat intracerebral hematomas, brain cysts and abscesses through an aspiration process.[5] First, a cerebral abscess is caused by inflammation and the aggregation of infected material, coming from local or remote infectious sources, within the brain tissue, such as an ear infection or lung infection, respectively. It may also be associated with congenital heart disease in young children. Possible factors in current high incidence include immunocompromised subpopulation, such as HIV, transplantation, or chemotherapy patients, and improved neuroimaging techniques that enable early diagnosis of abscesses. Traditional surgical treatment may result in excessive surgical trauma where edema is already present and may be inappropriate where abscesses are located at critical structures, in deeply seated eloquent regions, or in cases of multiple abscesses.[83] In contrast, CT or MRI-guided aspiration of brain abscesses provides therapeutic
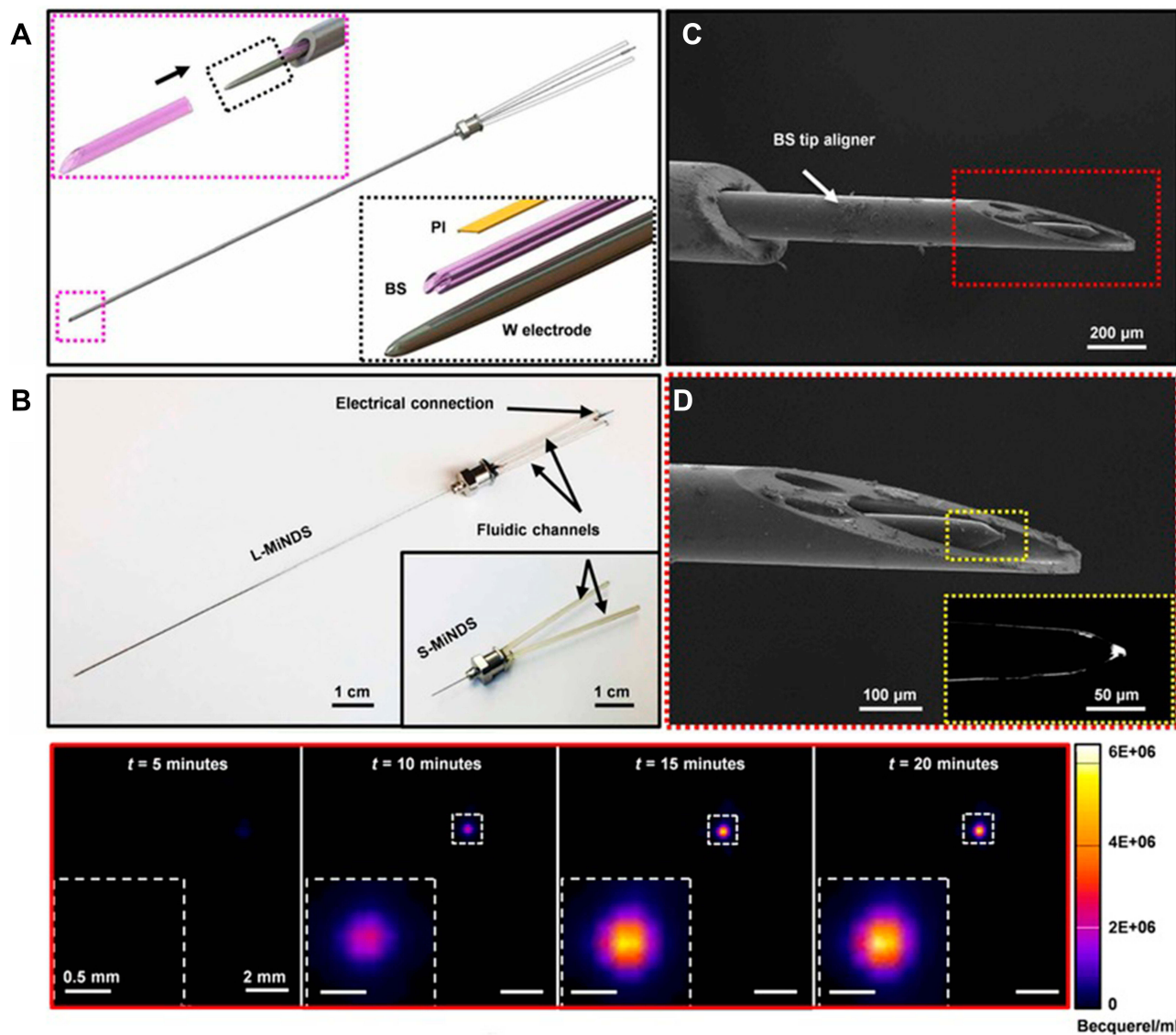
Figure 16 Miniaturized neural drug delivery system (MiNDS). (**A**) Schematic of system with key components shown in bottom-right inset; and borosilicate aligner tip depicted in top-left inset. (**B**) Depiction of long and short versions of MiNDS device: L-MiNDS and S-MiNDS, with electrical connection and fluidic channels identified. (**C, D**) Scanning electron microscopies. (**C**) SEM view of L-MiNDS tip. (**D**) SEM view of BS aligner tip. (**E**) PET images of diffusion of Cu-64 in vivo subsequent to MiNDS-mediated delivery in a rat. Images taken at 5, 10, 15, and 20 mins depict expression of Cu-64. Copyright © 2018. Reproduced with permission from Dagdeviren C, Ramadi KB, Joe P, et al. Miniaturized neural system for chronic, local intracerebral drug delivery. *Sci Transl Med*. 2018;10(425):eaan2742.[78]

value with no mortality and little morbidity. Boviatsis et al demonstrated CT-guided needle aspiration of cerebral abscesses.[83]

Meanwhile, intracerebral hemorrhage (ICH) is a particularly dangerous type of stroke with mortality in excess of 40%.[84] Recent work has emerged to address the invasiveness of open-craniotomy treatments based on minimally invasive strategies, achieving promising results in order to enable surgeons to better visualize blood clots and bleeding.[84] To address shortcomings in this area, Kellner et al proposed a neuroendoscopic hematoma treatment known as Stereotactic ICH Underwater Blood Aspiration (SCUBA). As shown in

Figure 17, SCUBA differs from competing ICH therapies in combining two neuroendoscopic phases, based, respectively, on dry and wet-field strategies.

Finally, needle aspiration has also been applied to treating cysts of the central nervous system. Liu et al exploited needle aspiration to 77 patients with cystic intracranial tumors, followed by Gamma Knife surgery.[85] 88.3% of patients showed improved symptoms immediately after cyst aspiration. The authors found that such a reduction of the volume of tumors improved the effectiveness of the Gamma Knife by enabling a higher radiation dose, while lowering the risk of complications.
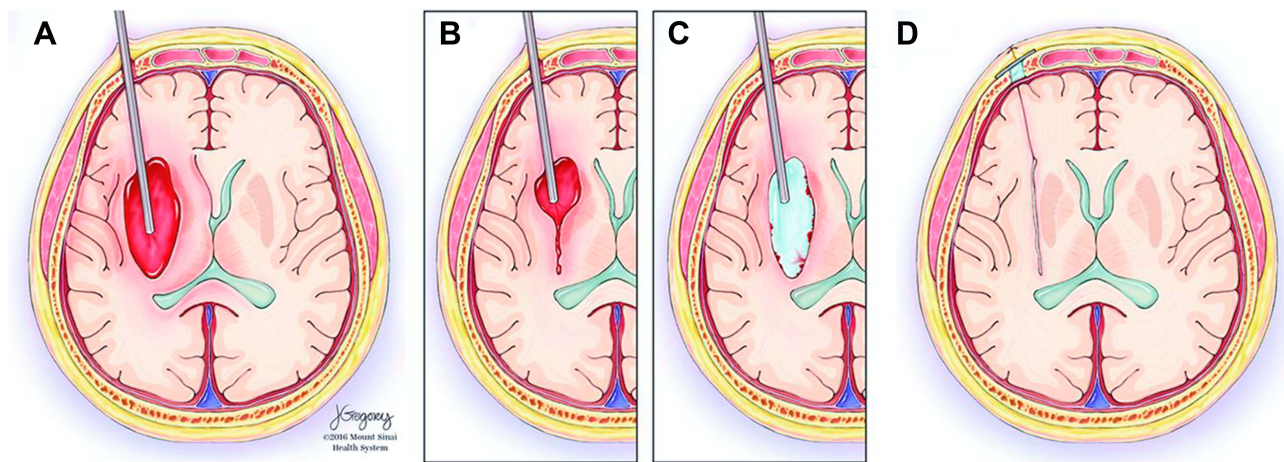
Figure 17 Stereotactic Intracerebral Hemorrhage Underwater Blood Aspiration (SCUBA) technique. (**A**) The cannula is inserted distally to the hematoma under stereotactic navigation. (**B**) Blood of the hematoma is aspirated as brain tissue closes in around the tip whereupon the cannula is retracted a few centimeters. (**C**) Subsequently, the surgeon infuses saline through the cannula, filling the cavity. (**D**) The saline is evacuated, and the cannula is fully retracted; intraoperative ultrasound and DYNA CT images are acquired to confirm the hematoma removal. Copyright © 2018. BMJ. Reproduced with permission from Kellner CP, Chartrain AG, Nistal DA, et al. The stereotactic intracerebral hemorrhage underwater blood aspiration (SCUBA) technique for minimally invasive endoscopic intracerebral hemorrhage evacuation. J Neurointerv Surg. 2018;10(8):771–776.[84]

Stereotactic Brachytherapy

Brachytherapy is a radiotherapy that involves implanting radioactive seeds into tumor tissue, as pioneered in 1901 by Pierre Curie.[86] In 1965, Iodine 125 was first applied to cancer therapy, namely for prostate, lung as well as lymph node cancers.[87] The development of brachytherapy in brain tumors is attributed to Mundinger,[6] based on the implantation of iridium-192 wires into gliomas in the early 1960s and iodine-125 seeds in 1979.[88,89] Currently, prevailing brachytherapy for brain tumors, which is limited to a few centers worldwide, is founded on iodine-125.[6]

Stereotactic brachytherapy involves seed implantation performed under general anesthesia.[6] The prevailent stereotactic approach involves fastening a frame the head of the patient and exploiting fiducials such as in Figure 13 for determining the image-to-patient transformation. Computerized treatment planning entails 3D image reconstruction and CT registration with MRI and/or PET datasets, culminating in the determination of the best implantation locations and trajectories in the coordinate system of the frame. The insertion of 4.5-mm-long iodine-125 seeds proceeds through catheters,[6] with each catheter inserted through a 2-millimeter cranial burr hole. A follow-up CT scan is scheduled the next day, whereby postoperative seed positions are tracked in relation to the preoperative planning. For temporary implants, seed removal takes place after 20–30 days under local anesthesia, without the need for stereotaxy.

Needle-Based Thermal Ablation

Recently, two techniques have been proposed for thermal ablation of brain tumors using a needle-like interstitial device. Monteris Medical's NeuroBlate system, depicted in Figure 18, features an elongated optic probe that delivers laser-based thermal therapy to brain tumors.[8,90,91] Medtronic has a similar system, called Visualase,[92] which works in the same way. These techniques are generally known as laser interstitial thermal therapy (LITT). Such as system can also ablate an epileptogenic zone, as proposed by Curry et al[93,94] Meanwhile, MacDonell et al have proposed a high-intensity focused ultrasound (HIFU) probe in conjunction with a robotic thermal ablation approach.[7] Real-time GPU-accelerated thermal monitoring for thermal ablation therapy of brain tumors has been proposed by Chen,[95] whihc is founded on an efficient computational algorithm, termed the nonlinear distorted Born iterative method (DIBM), for solving the electric volume integral equation.

Conclusions

This paper has provided both the clinical perspective and a brief survey of the major technical milestones in needle steering for neurosurgical applications. It is clear that the past and present of neurological needle therapies is straight and that its future, based on these milestones, is curvilinear. It is also apparent that progress in neurosurgical planning and simulation in general, building on progress in MRI pulse sequence development, particularly in diffusion imaging[96,97]
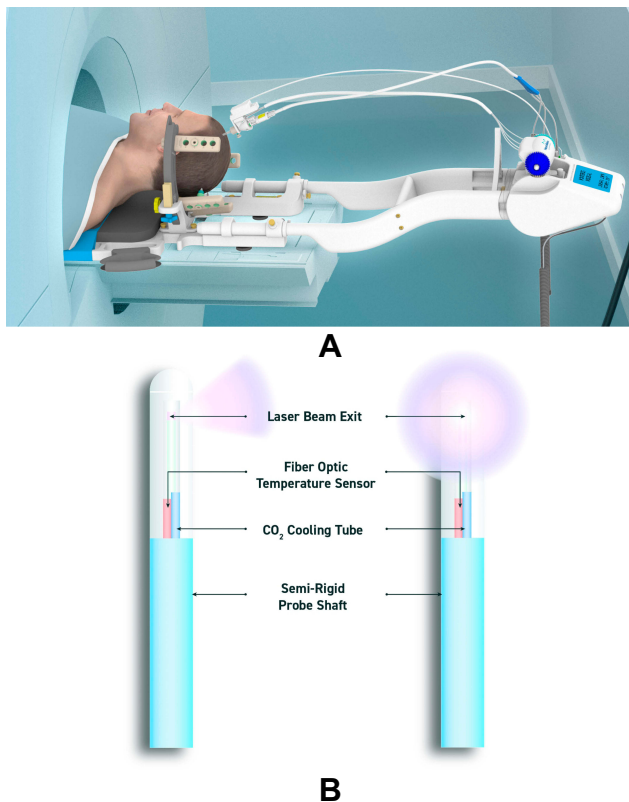
Figure 18 NeuroBlate commercial laser-based thermal ablation system for neurosurgical applications. (**A**) Robotic positioning system, enabling probe positioning from workstation during the procedure. (**B**) Two optic laser probes available for NeuroBlate: directional and diffusing tip probes.[8,90,91] Reproduced with permission from Monteris Medical. NeuroBlate® system. [Online] Available from: https://www.monteris.com/neuroblate-system/.[90]

(e.g. High-Angular Resolution Diffusion Imaging and related sequences) and functional imaging[98] (e.g. fMRI as a neurosurgery planning tool), and building on progress in segmentation, notably through deep learning methods,[99] promise to make neurosurgery planning and simulation much more descriptive, while improving patient outcome. These on-going revolutions in neurosurgery planning and simulation could potentiate novel use-cases for highly selective therapy delivery mechanisms that will be achievable with curvilinear needles, where these areas of research will reinforce each other symbiotically.

The other revolution that has occurred over time, in conjunction with the advent of the Internet, is the emergence of open-source software. There are myriad open-source software tools that can and will be brought to bear in ensuring that the curvilinear future is a safe one that the clinician can trust, starting with open-source surgery planning that includes Brigham Women's Hospital and Harvard's 3DSlicer platform,[100] featuring Slicer IGT for image-guided

therapy,[101] OpenIGTLink for communication and control of surgical robots,[102,103] and PLUS for ultrasound guidance,[104] as well as Medical Imaging Interaction Toolkit (MITK) produced by the German Cancer Research Center (DFKZ),[105] which also functions with some of 3D Slicer's components. Both of these surgery planning tools build on open-source visualization and medical image analysis developed by Kitware, namely the Visualization Toolkit (VTK)[106] and Insight Segmentation and Registration Toolkit (ITK).[107] Several open-source tools for robotic as well as tissue simulation are also relevant to this discussion, including OpenRAVE and OpenRobotics' Gazebo on the robot side,[108,109] and Simulation Open Framework Architecture (SOFA) and Kitware's Interactive Medical Simulation Toolkit.[110,111]

A key challenge will involve the integration of some of these open-source software tools, in order to achieve realistic patient-specific simulation and planning that instill clinical confidence, as well as lay a groundwork for animal trials and first-in-human trials. This integration will certainly necessitate important conversations, and the elaboration of meaningful requirements, based on interactions between robotics, biomechanics, and medical image analysis experts on one side and clinical early adopters comprised surgeons and physicians on the other.

Disclosure

The authors report no conflicts of interest in this work.

References

1. Perlmutter JS, Mink JW. Deep brain stimulation. *Annu Rev Neurosci*. 2006;29:229–257. doi:10.1146/annurev.neuro.29.051605.112824
2. Goldstein HE, Youngerman BE, Shao B, et al. Safety and efficacy of stereoelectroencephalography in pediatric focal epilepsy: a single-center experience. *J Neurosurg Pediatr*. 2018;22(4):444–452. doi:10.3171/2018.5.PEDS1856
3. Engh JA, Minhas DS, Kondziolka D, Riviere CN. Percutaneous intracerebral navigation by duty-cycled spinning of flexible bevel-tipped needles. *Neurosurgery*. 2010;67(4):1117–1122. doi:10.1227/NEU.0b013e3181ec1551
4. Chandrasoma PT, Smith MM, Apuzzo ML. Stereotactic biopsy in the diagnosis of brain masses: comparison of results of biopsy and resected surgical specimen. *Neurosurgery*. 1989;24(2):160–165. doi:10.1227/00006123-198902000-00002
5. Chen L, Dong L, She L, et al. Treatment of chronic subdural hematoma by novel YL-1 hollow needle aspiration drainage system (697 cases report). *Neurol Sci*. 2017;38(1):109–113. doi:10.1007/s10072-016-2717-4
6. Schwarz SB, Thon N, Nikolajek K, et al. Iodine-125 brachytherapy for brain tumours – a review. *Radiat Oncol*. 2012;7:30. doi:10.1186/1748-717X-7-30
7. MacDonell J, Patel N, Rubino S, et al. Magnetic resonance-guided interstitial high-intensity focused ultrasound for brain tumor ablation. *Neurosurg Focus*. 2018;44(2):E11. doi:10.3171/2017.11.FOCUS17613

8. Medical. Introducing NeuroBlate OPTIC laser probes. [Online]. Available from: https://www.monteris.com/wp-content/uploads/2019/11/AA10365-Rev-B.1-NeuroBlate-Technical-Brochure-1-1.pdf. Accessed February 20, 2020.

9. Reed KB, Majewicz A, Kallem V, et al. Robot-assisted needle steering. *IEEE Robot Autom Mag*. 2011;18(4):35–46. doi:10.1109/MRA.2011.942997

10. Cowan J, Goldberg K, Chirikjian GS, et al. Robotic needle steering: design, modeling, planning, and image guidance. In: Rosen J, Hannaford B, Satava R, editors. *Surgical Robotics - Systems, Applications, and Visions. s.l.* Springer; 2011:557–582.

11. Miller K, Joldes G, Lance D, Wittek A. Total lagrangian explicit dynamics finite element algorithm for computing soft tissue deformation. *Commun Numer Meth Eng*. 2007;23:121–134. doi:10.1002/cnm.887

12. Drakopoulos F, Foteinos P, Liu Y, Chrisochoides NP. Toward a real time multi-tissue adaptive physics-based non-rigid registration framework for brain tumor resection. *Front Neuroinform*. 2014;8:11. doi:10.3389/fninf.2014.00011

13. Audette MA, Chernikov AN, Chrisochoides NP,. A review of mesh generation for medical simulators. In: Sokolowski JA, Banks CM, editors. *Handbook of Real-World Applications in Modeling and Simulation*; 2012. doi:10.1002/9781118241042.ch7

14. Webster RJ, Kim JS, Cowan NJ, Chirikjian GS, Okamura AM. Nonholonomic modeling of needle steering. *Int J Rob Res*. 2006;25(5–6):509–525. doi:10.1177/0278364906065388

15. Reed KB, Kallem V, Alterovitz R, Goldberg K, Okamura AM, Cowan NJ. Integrated planning and image-guided control for planar needle steering. Proceeding IEEE RAS & EMBS International Conference on Biomedical Robotics and Biomechatronics; October 19, 2008; Pisa, Italy. 819–824.

16. Konh B, Honarvar M, Hutapea P Application of SMA wire for an active steerable cannula. ASME Conference Smart Materials, Adaptive Structures and Intelligent Systems, SMASIS 2; 2013.

17. Okazawa S, Ebrahimi R, Chuang J, Salcudean S, Rohling R. Hand-held steerable needle device. *IEEE ASME Trans Mechatron*. 2005;10:285–296. doi:10.1109/TMECH.2005.848300

18. Dupont PE, Lock JL, Itkowitz B, Butler E. Design and control of concentric-tube robots. *IEEE Trans Robot*. 2010;26(2):209–225. doi:10.1109/TRO.2009.2035740

19. Rucker DC, Webster RJ 3rd, Chirikjian GS, Cowan NJ. Equilibrium conformations of concentric-tube continuum robots. *Int J Rob Res*. 2010;29(10):1263–1280. doi:10.1177/0278364910367543

20. DiMaio SP, Salcudean SE. Needle steering and motion planning in soft tissues. *IEEE Trans Biomed Eng*. 2005;52(6):965–974. doi:10.1109/TBME.2005.846734

21. Glozman D, Shoham M. Image-guided robotic flexible needle steering. *IEEE Trans Rob*. 2007;23:459–467. doi:10.1109/TRO.2007.898972

22. Mallapragada VG, Sarkar N, Podder TK. Robot-assisted real-time tumor manipulation for breast biopsy. *IEEE Trans Robot*. 2009;25(2):316–324. doi:10.1109/TRO.2008.2011418

23. Winters BS, Shepard SR, Foty RA. Biophysical measurement of brain tumor cohesion. *Int J Cancer*. 2005;114(3):371–379. doi:10.1002/(ISSN)1097-0215

24. Park W, Kim JS, Zhou Y, Cowan NJ, Okamura AM, Chirikjian GS. *Diffusion-based motion planning for a nonholonomic flexible needle model*. Proc. IEEE International Conference on Robotics and Automation; Barcelona, Spain; 2005:4600–4605.

25. Luca AD, Oriolo G,. Modelling and control of nonholonomic mechanical systems. Kinematics and dynamics of multi-body systems. In: Angeles J, Kecskeméthy A, editors. *CISM International Centre for Mechanical Sciences (Courses and Lectures)*. Vol. 360. Vienna: Springer; 1995. doi:10.1007/978-3-7091-4362-9_7

26. Abolhassani N, Patel RV, Ayazi F. Minimization of needle deflection in robot-assisted percutaneous therapy. *Int J Med Robot*. 2007;3(2):140–148. doi:10.1002/(ISSN)1478-596X

27. Abolhassani N, Patel R, Moallem M. Trajectory generation for robotic needle insertion in soft tissue. *Conf Proc IEEE Eng Med Biol Soc*. 2004;4:2730–2733. doi:10.1109/IEMBS.2004.1403782

28. Abolhassani N, Patel RV. Deflection of a flexible needle during insertion into soft tissue. *Conf Proc IEEE Eng Med Biol Soc*. 2006;1:3858–3861.

29. Alterovitz R, Branicky M, Goldberg K. Motion planning under uncertainty for image-guided medical needle steering. *Int J Rob Res*. 2008;27(11–12):1361–1374. doi:10.1177/0278364908097661

30. Alterovitz R, Lim A, Goldberg K, Chirikjian G, Okamura A. Steering flexible needles under Markov motion uncertainty. *Intell Rob Syst*. 2005;1570–1575.

31. Chinzei K, Hata H, Jolesz FA, Kikinis R. *MRI Compatible Surgical Assist Robot: System Integration and Preliminary Feasibility Study*. Vol. 1935. Springer, MICCAI; 2000:921–930.

32. Fischer GS, Cole GA, Pilitsis JG System and method for robotic surgical intervention. 12/873,152, US Patent Application. 2010 Aug.

33. Sutherland GR, Latour I, Greer AD, Fielding T, Feil G, Newhook P. An image-guided magnetic resonance-compatible surgical robot. *Neurosurgery*. 2008;62(2):286–292. doi:10.1227/01.neu.0000315996.73269.18

34. NeuroArm. Project. [Online]. Available from: http://www.neuroarm.org/project/. Accessed December 20, 2019.

35. Cole G, Pilitsis J, Fischer GS,. Design of a robotic system for MRI-guided deep brain stimulation electrode placement. International Conference on Robotics and Automation; 2009; Kobe, Japan. 4450–4456.

36. Chakravarty MM, Sadikot AF, Mongia S, Bertrand G, Collins DL. Towards a multi-modal atlas for neurosurgical planning. *Med Image Comput Comput Assist Interv*. 2006;9(Pt2):389–396. doi:10.1007/11866763_48

37. Rashid T, Sultana S, Fischer GS, Pilitsis JG, Audette MA. *Deformable Multi-Material 2-Simplex Surface Mesh for Intraoperative MRI-Ready Surgery Planning and Simulation, with Deep-Brain Stimulation Applications*. Quebec City, Canada: MICCAI BIVPCS/POCUS 94-102; 2017.

38. Huang J, Chen C, Axel L. Fast multi-contrast MRI reconstruction. *Med Image Comput Comput Assist Interv*. 2012;15(Pt1):281–288. doi:10.1007/978-3-642-33415-3_35

39. Deoni SC, Josseau MJ, Rutt BK, Peters TM. *Visualization of thalamic nuclei on high resolution, multi-averaged T1 and T2 maps acquired at 1.5 T. Hum Brain Mapp*. 2005;25(3):353–359. doi:10.1002/hbm.20117

40. Xiao Y 1, Beriault S, Pike GB, Collins DL. Multicontrast multiecho FLASH MRI for targeting the subthalamic nucleus. *Magn Reson Imaging*. 2012;30(5):627–640. doi:10.1016/j.mri.2012.02.006

41. Alterovitz R, Goldberg K, Okamura AM. *Planning for steerable bevel-tip needle insertion. Proceeding IEEE International Conference on Robotics and Automation*. Barcelona, Spain; 2005:1652–1657

42. Chentanez N, Alterovitz R, Ritchie D, et al. Interactive simulation of surgical needle insertion and steering, Prof. ACM SIGGRAPH; 2009; New Orleans, LA, USA. 1–10.

43. Bui HP, Tomar S, Courtecuisse H, Audette M, Cotin S, Bordas SPA. Controlling the error on target motion through real-time mesh adaptation: applications to deep brain stimulation. *Int j Numer Method Biomed Eng*. 2018;34(5):e2958. doi:10.1002/cnm.2958

44. Bui HP, Tomar S, Courtecuisse H, Cotin S, Bordas SPA. Real-time error control for surgical simulation. *IEEE Trans Biomed Eng*. 2018;65(3):596–607. doi:10.1109/TBME.2017.2695587

45. Courtecuisse H, Allard J, Kerfriden P, Bordas SP, Cotin S, Duriez C. Real-time simulation of contact and cutting of heterogeneous soft-tissues. *Med Image Anal*. 2014;18(2):394–410. doi:10.1016/j.media.2013.11.001

46. Bui HP, Tomar S, Bordas SPA. Corotational cut finite element method for real-time surgical simulation: application to needle insertion simulation. *Comput Methods Appl Mech Eng*. 2019;345:183–211. doi:10.1016/j.cma.2018.10.023

47. Xu J, Wang L, Wong KCL, Shi P A meshless framework for bevel-tip flexible needle insertion through soft tissue. IEEE RAS & EMBS Int. Conf. Biomedical Robotics and Biomechatronics. Tokyo; 2010:753–758.

48. Rappel H, Beex LAA, Hale JS, Noels L, Bordas SPA. *A tutorial on bayesian inference to identify material parameters in solid mechanics*s. *Arch Computat Methods Eng*. 2019. doi:10.1007/s11831-018-09311-x

49. Rappel H, Beex L, Bordas S. *Bayesian inference to identify parameters in viscoelasticity*. *Mech Time-Depend Mater*. 2017;22. doi:10.1007/s11043-017-9361-0

50. Rappel H, Beex LAA. Estimating fibres' material parameter distributions from limited data with the help of bayesian inference. *Eur J Mech a Solids*. 2019;75:169–196. doi:10.1016/j.euromechsol.2019.01.001

51. Mohamedou M, Zulueta K, Chung CN, et al. Bayesian identification of mean-field homogenization model parameters and uncertain matrix behavior in non-aligned short fiber composites. *Compos Struct*. 2019;220:64–80. doi:10.1016/j.compstruct.2019.03.066

52. Hauseux P, Hale JS, Bordas SPA. Accelerating Monte Carlo estimation with derivatives of high-level finite element models. *Comput Methods Appl Mech Eng*. 2017;318:917–936. doi:10.1016/j.cma.2017.01.041

53. Hauseux P, Hale JS, Bordas SPA. Calculating the malliavin derivative of some stochastic mechanics problems. *PLoS One*. 2017;12 (12):e0189994. doi:10.1371/journal.pone.0189994

54. Hauseux P, Hale JS, Cotin S, Bordas SPA. Quantifying the uncertainty in a hyperelastic soft tissue model with stochastic parameters. *Appl Math Model*. 2018;62:86–102. doi:10.1016/j.apm.2018.04.021

55. Olivi A, Weingart JD, Liauw J, Raza SM. *Frame and Frameless Stereotactic Brain Biopsy. Youmans and Winn Neurological Surgery. 7th* ed. s.l: Elsevier; 2016:942–948.

56. Tilgner J, Herr M, Ostertag C, Volk B. Validation of intraoperative diagnoses using smear preparations from stereotactic brain biopsies: intraoperative versus final diagnosis–influence of clinical factors. *Neurosurgery*. 2005;56(2):257–265. doi:10.1227/01.NEU.0000148899.39020.87

57. Leksell L. A stereotaxic apparatus for intracerebral surgery. *Acta Chir Scand*. 1949;99:229–233.

58. Brown RA. A stereotactic head frame for use with CT body scanners. *Invest Radiol*. 1979;14:300–304. doi:10.1097/00004424-197907000-00006

59. Leksell L, Leksell D, Schwebel J. Stereotaxis and nuclear magnetic resonance. *J Neurol Neurosurg Psychiatry*. 1985;48:14–18. doi:10.1136/jnnp.48.1.14

60. Krieger MD, Chandrasoma PT, Zee C-S, et al. Role of stereotactic biopsy in the diagnosis and management of brain tumors. *Semin Surg Oncol*. 1998;14:13–25. doi:10.1002/(ISSN)1098-2388

61. Trippel M, Nikkhah G. Stereotactic neurosurgical treatment options for craniopharyngioma. Front Endocrinol (Lausanne). 2012;3:63. doi: 10.3389/fendo.2012.00063

62. Lemieux L, Jagoe R. Effect of fiducial marker localization on stereotactic target coordinate calculation in CT slices and radiographs. *Phys Med Biol*. 1994;39(11):1915–1928. doi:10.1088/0031-9155/39/11/008

63. BrainLab. Cranial navigation application. [Online]. Available from: https://www.brainlab.com/surgery-products/overview-neurosurgery-products/cranial-navigation/. Accessed December 20, 2019.

64. Medtronic. Stealth navigation for neurosurgery. [Online] Available from: https://www.medtronic.com/us-en/healthcare-professionals/products/neurological/surgical-navigation-systems.html. Accessed December 20, 2019.

65. Quiñones-Hinojosa A 1, Ware ML, Sanai N, McDermott MW. Assessment of image guided accuracy in a skull model: comparison of frameless stereotaxy techniques vs. frame-based localization. *J Neurooncol*. 2006;76(1):65–70. doi:10.1007/s11060-005-2915-z

66. Wikipedia. Stereotactic surgery. Available from: https://en.wikipedia.org/wiki/Stereotactic_surgery. Accessed February 20, 2020.

67. Kongkham PN, Knifed E, Tamber MS, Bernstein M. Complications in 622 cases of frame-based stereotactic biopsy, a decreasing procedure. *Can J Neurol Sci*. 2008;35(1):79–84. doi:10.1017/S0317167100007605

68. Sierens DK, Kutz S, Pilitsis JG, Bakay RAE. Stereotactic Surgery with Microelectrode Recordings. [book auth.]. In: Bakay RAE, editor. *Movement Disorders: The Essentials*. Thieme; 2008:83–114.

69. Lyons KE, Wilkinson SB, Overman JB, Pahwa R. Surgical and hardware complications of subthalamic stimulation A series of 160 procedures. *Neurol*. 2004;63:612–616. doi:10.1212/01.WNL.0000134650.91974.1A

70. Ewert S, Plettig P, Li N, et al. Toward defining deep brain stimulation targets in MNI space: a subcortical atlas based on multimodal MRI, histology and structural connectivity. *Neuroimage*. 2018;170:271–282. doi:10.1016/j.neuroimage.2017.05.015

71. Butson CR, Cooper SE, Henderson JM, McIntyre CC. Patient-specific analysis of the volume of tissue activated during deep brain stimulation. *Neuroimage*. 2007;34(2):661–670. doi:10.1016/j.neuroimage.2006.09.034

72. McIntyre CC 1, Grill WM, Sherman DL, Thakor NV. Cellular effects of deep brain stimulation: model-based analysis of activation and inhibition. *J Neurophysiol*. 2004;91(4):1457–1469. doi:10.1152/jn.00989.2003

73. Zhang Q, Kim Y-C and Narayanan NS. Disease-modifying therapeutic directions for Lewy-Body dementias. *Front. Neurosci*. 2015;9:293. doi: 10.3389/fnins.2015.00293

74. Thalamus-schematic-de.svg. Available from: https://commons.wikimedia.org/wiki/File:Thalamus-schematic-de.svg. Accessed February 20, 2020.

75. Subthalamic nucleus. Available from: https://en.wikipedia.org/wiki/Subthalamic_nucleus#/media/File:Basal-ganglia-coronal-sections-large.png. Accessed February 20, 2020.

76. National Institute on Drug Abuse. Public Domain Picture: Brain reward pathway. Available from http://www.publicdomainfiles.com/show_file.php?id=13989816622720. Accessed February 20, 2020.

77. Wang J, Wang Q, Wang M, et al. Occipital lobe epilepsy with ictal fear: evidence from a stereo-electroencephalography (sEEG) case. *Front Neurol*. 2018;9:644. doi:10.3389/fneur.2018.00644

78. Dagdeviren C, Ramadi KB, Joe P, et al. Miniaturized neural system for chronic, local intracerebral drug delivery. *Sci Transl Med*. 2018;10(425):eaan2742. doi:10.1126/scitranslmed.aan2742

79. Kalamangalam GP, Tandon N. Stereo-EEG implantation strategy. *J Clin Neurophysiol*. 2016;33(6):483–489. doi:10.1097/WNP.0000000000000254

80. González-Martínez J, Bulacio J, Thompson S, et al. Technique, results, and complications related to robot-assisted stereoelectroencephalography. *Neurosurgery*. 2016;78(2):169–180. doi:10.1227/NEU.0000000000001034

81. Souweidane MM, Kramer K, Pandit-Taskar N, et al. Convection-enhanced delivery for diffuse intrinsic pontine glioma: a single-centre, dose-escalation, Phase 1 trial. *Lancet Oncol*. 2018;19(8):1040–1050. doi:10.1016/S1470-2045(18)30322-X

82. UCSF Brain Center. Convection enhanced delivery. [Online] Available from: https://braintumorcenter.ucsf.edu/treatment/experimental-diagnostics-therapies/convection-enhanced-delivery. Accessed December 20, 2019.

83. Boviatsis EJ, Kouyialis AT, Stranjalis G, Korfias S, Sakas DE. CT-guided stereotactic aspiration of brain abscesses. *Neurosurg Rev*. 2003;26(3):206–209. doi:10.1007/s10143-003-0257-x

84. Kellner CP, Chartrain AG, Nistal DA, et al. The stereotactic intracerebral hemorrhage underwater blood aspiration (SCUBA) technique for minimally invasive endoscopic intracerebral hemorrhage evacuation. *J Neurointerv Surg*. 2018;10(8):771–776. doi:10.1136/neurintsurg-2017-013719

85. Liu X, Yu Q, Zhang Z, et al. Same-day stereotactic aspiration and Gamma Knife surgery for cystic intracranial tumors. *J Neurosurg*. 2012;117(Suppl):45–48. doi:10.3171/2012.7.GKS121019

86. Holm HH, Strøyer I, Hansen H, Stadil F. Ultrasonically guided percutaneous interstitial implantation of iodine 125 seeds in cancer therapy. *Br J Radiol*. 1981;54(644):665–670. doi:10.1259/0007-1285-54-644-665

87. Kim JH, Hilaris B. Iodine 125 source in interstitial tumor therapy. Clinical and biological considerations. *Am J Roentgenol Radium Ther Nucl Med*. 1975;123(1):163–169. doi:10.2214/ajr.123.1.163

88. Mundinger F, Ostertag CB, Birg W, Weigel K. Stereotactic treatment of brain lesions. Biopsy, interstitial radiotherapy (iridium-192 and iodine-125) and drainage procedures. *Appl Neurophysiol*. 1980;43(3–5):198–204.

89. Bernstein M, Gutin PH. Interstitial irradiation of brain tumors: a review. *Neurosurgery*. 1981;9(6):741–750. doi:10.1227/00006123-198112000-00022

90. Monteris Medical. NeuroBlate® system. [Online] Available from: https://www.monteris.com/neuroblate-system/. Accessed February 20, 2020.

91. Monteris Medical. NeuroBlate® system disposables. [Online] Available from: https://www.monteris.com/neuroblate-system-disposables/. Accessed February 20, 2020.

92. Medtronic. Visualase MRI-guided laser ablation. [Online] Available from: https://www.medtronic.com/us-en/healthcare-professionals/products/neurological/laser-ablation/visualase.html. Accessed December 20, 2019.

93. North RY, Raskin JS, Curry DJ. MRI-guided laser interstitial thermal therapy for epilepsy. *Neurosurg Clin N Am*. 2017;28(4):545–557. doi:10.1016/j.nec2017.06.001

94. Boerwinkle VL, Mohanty D, Foldes ST, et al. Correlating resting-state fMRI connectivity by independent component analysis-based epileptogenic zones with intracranial electroencephalogram localizes seizure onset zones and surgical outcomes in prospective pediatric intractable epilepsy study. *Brain Connect*. 2017;7(7):424–442. doi:10.1089/brain.2016.0479

95. Chen G, Stang J, Haynes M, Leuthardt E, Moghaddam M. Real-time three-dimensional microwave monitoring of interstitial thermal therapy. *IEEE Trans Biomed Eng*. 2018;65(3):528–538. doi:10.1109/TBME.2017.2702182

96. Maier-Hein KH, Neher PF, Descoteaux M, et al. The challenge of mapping the human connectome based on diffusion tractography. *Nat Commun*. 2017;8(1):1349. doi:10.1038/s41467-017-01285-x

97. Vaillancourt O, Girard G, Bore A, Descoteaux M. A fiber navigator for neurosurgical planning (NeuroPlanningNavigator). *Organ Hum Brain Mapp*. 2010;1.

98. Nadkarni TN, Andreoli MJ, Prabhakaran V, et al. Usage of fMRI for pre-surgical planning in brain tumor and vascular lesion patients: task and statistical threshold effects on language lateralization. *Neuroimage Clin*. 2014;7:415–423. doi:10.1016/j.nicl.2014.12.014

99. Litjens G, Kooi T, Bejnordi BE, et al. A survey on deep learning in medical image analysis. *Med Image Anal*. 2017;42:60–88. doi:10.1016/j.media.2017.07.005

100. BWH. 3D slicer. [Online]. Available from: https://www.slicer.org/. Accessed December 20, 2019.

101. Queen's University. Slicer IGT. [Online]. Available from: http://www.slicerigt.org/wp/. Accessed December 20, 2019.

102. Tokuda J, Fischer GS, Papademetris X, et al. OpenIGTLink: an open network protocol for image-guided therapy environment. *Int J Med Robot*. 2009;5(4):423–434. doi:10.1002/rcs.274

103. Arata J, Kozuka H, Kim HW, et al. Open core control software for surgical robots. *Int J Comput Assist Radiol Surg*. 2010;5(3):211–220. doi:10.1007/s11548-009-0388-9

104. Lasso A, Heffter T, Rankin A, Pinter C, Ungi T, Fichtinger G. PLUS: open-source toolkit for ultrasound-guided intervention systems. *IEEE Trans Biomed Eng*. 2014;61(10):2527–2537. doi:10.1109/TBME.2014.2322864

105. DFKZ. The medical imaging interaction toolkit (MITK). [Online] Available from: http://mitk.org. Accessed December 20, 2019.

106. Kitware. The visualization toolkit. [Online]. Available from: vtk.org. Accessed December 20, 2019.

107. Kitware Insight segmentation and registration toolkit (ITK). [Online]. Available from: itk.org. Accessed December 20, 2019.

108. OpenRAVE. Open robotics automation virtual environment. [Online]. Available from: openrave.org. Accessed December 20, 2019.

109. Open Robotics. Gazebo. [Online]. Available from: gazebosim.org. Accessed December 20, 2019.

110. SOFA. Simulation open framework architecture. [Online] Available from: www.sofa-framework.org. Accessed December 20, 2019.

111. Kitware. Interactive medical simulation toolkit. [Online]. Available from: www.imstk.org. Accessed December 20, 2019.